

Article

# TiO<sub>2</sub>-Modified Montmorillonite-Supported Porous Carbon-Immobilized Pd Species Nanocomposite as an Efficient Catalyst for Sonogashira Reactions

Yuli Chen <sup>1</sup>, Kailang Sun <sup>1</sup>, Taojun Zhang <sup>1</sup>, Jie Zhou <sup>1</sup>, Yonghong Liu <sup>1</sup>, Minfeng Zeng <sup>1,\*</sup>,<sup>†</sup> , Xiaorong Ren <sup>1</sup>, Ruokun Feng <sup>1</sup>, Zhen Yang <sup>1,\*</sup>,<sup>†</sup>, Peng Zhang <sup>2</sup>, Baoyi Wang <sup>2</sup> and Xingzhong Cao <sup>2,\*</sup>,<sup>†</sup> 

<sup>1</sup> Research Center of Advanced Catalytic Materials and Functional Molecular Synthesis, Zhejiang Key Laboratory of Alternative Technologies for Fine Chemicals Process, College of Chemistry and Chemical Engineering, Shaoxing University, Shaoxing 312000, China

<sup>2</sup> Institute of High Energy Physics, Chinese Academy of Sciences, Beijing 100049, China

\* Correspondence: zengmf@usx.edu.cn (M.Z.); yangzhen09@usx.edu.cn (Z.Y.); caoxzh@ihep.ac.cn (X.C.)

† These authors contributed equally to this work.

**Abstract:** In this study, a combination of the porous carbon (PCN), montmorillonite (MMT), and TiO<sub>2</sub> was synthesized into a composite immobilized Pd metal catalyst (TiO<sub>2</sub>-MMT/PCN@Pd) with effective synergism improvements in catalytic performance. The successful TiO<sub>2</sub>-pillaring modification for MMT, derivation of carbon from the biopolymer of chitosan, and immobilization of Pd species for the prepared TiO<sub>2</sub>-MMT/PCN@Pd<sup>0</sup> nanocomposites were confirmed using a combined characterization with X-ray diffraction (XRD), Fourier transform infrared spectroscopy (FTIR), N<sub>2</sub> adsorption–desorption isotherms, high-resolution transition electron microscopy (HRTEM), X-ray photoelectron spectroscopy (XPS), and Raman spectroscopy. It was shown that the combination of PCN, MMT, and TiO<sub>2</sub> as a composite support for the stabilization of the Pd catalysts could synergistically improve the adsorption and catalytic properties. The resultant TiO<sub>2</sub>-MMT<sub>80</sub>/PCN<sub>20</sub>@Pd<sup>0</sup> showed a high surface area of 108.9 m<sup>2</sup>/g. Furthermore, it exhibited moderate to excellent activity (59–99% yield) and high stability (recyclable 19 times) in the liquid–solid catalytic reactions, such as the Sonogashira reactions of aryl halides (I, Br) with terminal alkynes in organic solutions. The positron annihilation lifetime spectroscopy (PALS) characterization sensitively detected the development of sub-nanoscale microdefects in the catalyst after long-term recycling service. This study provided direct evidence for the formation of some larger-sized microdefects during sequential recycling, which would act as leaching channels for loaded molecules, including active Pd species.

**Keywords:** Sonogashira reactions; heterogeneous catalysis; structure–performance relations; positron annihilation



**Citation:** Chen, Y.; Sun, K.; Zhang, T.; Zhou, J.; Liu, Y.; Zeng, M.; Ren, X.; Feng, R.; Yang, Z.; Zhang, P.; et al. TiO<sub>2</sub>-Modified Montmorillonite-Supported Porous Carbon-Immobilized Pd Species Nanocomposite as an Efficient Catalyst for Sonogashira Reactions. *Molecules* **2023**, *28*, 2399. <https://doi.org/10.3390/molecules28052399>

Academic Editors: Maria Luisa Di Gioia, Luisa Margarida Martins and Isidro M. Pastor

Received: 1 February 2023

Revised: 26 February 2023

Accepted: 2 March 2023

Published: 6 March 2023



**Copyright:** © 2023 by the authors. Licensee MDPI, Basel, Switzerland. This article is an open access article distributed under the terms and conditions of the Creative Commons Attribution (CC BY) license (<https://creativecommons.org/licenses/by/4.0/>).

## 1. Introduction

Pd-based catalysts play important roles in many chemical transformations. In most applications, the homogeneous Pd catalyst contains not only the active Pd species but also various necessary ligands. Such homogeneous catalysis processes often suffer the difficulties of separation of the catalysts and ligands, recovery of the catalysts, and purity of the products, which make the processes un-green and cost-effective [1–4]. Therefore, the immobilization of active Pd species on appropriate supports to develop heterogeneous catalysts has received increasing attention both in the academic and industrial fields [5,6].

Recently, a variety of supports, such as active carbon, zeolites, MOFs, magnetic materials, clay, inorganic oxides (such as Al<sub>2</sub>O<sub>3</sub>, SiO<sub>2</sub>, TiO<sub>2</sub>, etc.), and organic polymers, have been attempted to immobilize Pd species to create heterogeneous catalyst systems [7–13]. Among these supports, active carbon is one of the most extensively investigated supporting materials owing to its high adsorption, good chemical inertness, and satisfied chelation.

However, most pores contained in the conventional activated carbons are at the microporous level (<2 nm), which limits the transfer efficiency of large-sized reactant and product molecules into and out of the pores [14,15]. Therefore, the introduction of additional larger-sized porous structures is required for the porous carbon supports. The most frequently used modification method is adding hard or soft templates to induce abundant meso-/macro-porous structure. For examples, after removing the templates of polyether and/or colloidal SiO<sub>2</sub> using pyrolysis or HF etching [16–19], the prepared porous carbon-supported Pd catalysts show a high mesoporous structure with high catalysis efficiency and stability as applied in coupling reactions. However, the added templates are required to be removed completely, leading to a complicated and un-economical preparation process. Hybridizing with other mesoporous materials such as montmorillonite (MMT) has been proven as another effective strategy to improve the adsorption capacity [20–23].

MMT clay [24] is a kind of abundant clay mineral in nature with a layered porous structure. The MMT layer consists of a central alumina octahedron sheet and two silicon tetrahedral sheets. Al<sup>3+</sup> and Si<sup>4+</sup> within the lattice structure are easily substituted by other ions with lower valence such as Mg<sup>2+</sup>, resulting in negative charges on the MMT layers. Moreover, they are often compensated by exchangeable positive cations, such as Na<sup>+</sup> and Ca<sup>2+</sup>. Driven by ion exchange or hydrogen-bonding interactions, many natural macromolecules can be easily intercalated into the MMT layers. After further hydrothermal carbonization, the natural macromolecules-derived porous carbon (PCN) can be well supported on the MMT matrices. For example, Pei et al. [25] prepared novel MMT-supported porous carbon (PCN) nanosphere adsorbents (with glucose as the carbon source) using a hydrothermal carbonization and chemical activation treatment with ZnCl<sub>2</sub>. The prepared MMT-PCN adsorbent exhibited an excellent performance of 686.94 mg·g<sup>-1</sup> for the removal of methylene blue (MB). Zhou et al. [26] also reported other novel MMT-supported PCN nanocomposites (derived from cellulose) with an adsorption capacity for the removal of MB of 138.1 mg·g<sup>-1</sup>. Besides the often-used carbon source of glucose and cellulose with totally carbon chains, other N-containing natural polymers such as chitosan (CS) have received increasing attention [27–29]. CS is a polycation under acidic conditions, and it can easily intercalate into the MMT layers through the ion exchange process. Its macromolecular backbone contains plenty of amino groups, and the derived PCN definitely contains a high content of the N heteroatom. The introduction of the N heteroatom into carbon lattices effectively modifies its surface physicochemical properties and brings new opportunities to improve their catalytic properties. MMT-supported CS-derived N-doped PCN has been demonstrated as a good supporting material for Pd metals [30].

However, natural MMT has limited porous structure, layer spacing, and cation exchange capacity. Pillaring modification of MMT can effectively improve these properties [31–34]. The polycationic precursors for metal oxides, such as Al<sub>2</sub>O<sub>3</sub>, Fe<sub>2</sub>O<sub>3</sub>, TiO<sub>2</sub>, ZrO<sub>2</sub>, Cr<sub>2</sub>O<sub>3</sub>, etc., that can form multi nucleus upon the hydrolysis process, can often be used as pillaring reagents to keep the MMT layers apart and prevent collapse. Among the different kinds of pillared MMT, TiO<sub>2</sub>-pillared MMT [35–40] has been proven as one of the most suitable supports for active species as applied in especially gas–solid catalytic reactions, based on its excellent characteristics: expanded interlayer spaces, large surface area, high porous structure, and pore size tunable from the micro- to meso-pore range. Recently, mesoporous TiO<sub>2</sub>-modified active carbon has been used as a novel support for Pd species. Xiao et al. [41] used TiO<sub>2</sub>-supported CS-derived carbon as a support to prepare novel Pd@TiO<sub>2</sub>/N-doped C catalysts, which exhibited high catalytic efficiency and stability for the hydrogenation of vanillin to 2-methoxy-4-methylphenol. It was also found that the carbonization of the CS component within the Al-pillared MMT/CS@Pd catalyst was in favor of further improvement of the comprehensive catalytic performance [42,43]. Based on these studies, it is expected that a combination of porous carbon, TiO<sub>2</sub>, and TiO<sub>2</sub>-pillaring modified MMT should be another novel promising support for Pd species. However, to the best of our knowledge, the preparation of porous carbon modified with both pillared MMT

and TiO<sub>2</sub>-supported stabilized Pd (TiO<sub>2</sub>-MMT/PCN@Pd) catalysts applied in liquid–solid heterogeneous coupling reactions has been reported in few studies.

In this study, a series of TiO<sub>2</sub>-modified MMT-supported PCN-stabilized Pd nanocomposites were synthesized (using CS as a carbon source), followed with fine microstructure characterizations and catalytic performance tests for the Sonogashira coupling reactions between aryl halides and terminal phenyl acetylene. The aim was to evaluate the synergism effects of the combination of PCN, MMT, and TiO<sub>2</sub> as a composite support for the stabilization of Pd catalysts as applied in liquid–solid organic reactions. The correlations between the microstructure and catalytic performance of the prepared novel catalytic nanocomposites were discussed. In addition, comparisons were made of the prepared novel catalysts with other recent solid-supported palladium catalysts in the Sonogashira reaction [44].

## 2. Results and Discussion

### 2.1. Microstructure of the Catalytic Nanocomposites

The XRD patterns of the starting Na-MMT, TiO<sub>2</sub>-MMT, and TiO<sub>2</sub>-MMT/PCN@Pd nanocomposites are shown in Figure 1a,b. For Na-MMT, the diffraction (001) peak that is attributed to the ordering of the MMT layers locates at the 2θ around 7.35°, related to the basal space of 1.20 nm. Considering that the thickness of the MMT layer itself is about 0.96 nm [45,46], the interlayer spacing distance of the starting Na-MMT is about 0.24 nm. The pillaring process involves the cations exchange of the polyhydroxy-Ti<sup>4+</sup> species exchanged with Na<sup>+</sup>, which props open the silicate layers. Upon high temperature treatment, the intercalated polyhydroxy-Ti<sup>4+</sup> species are transformed into TiO<sub>2</sub> nanoparticles, linking permanently with the silicate layers. As a result, for the TiO<sub>2</sub>-MMT and the TiO<sub>2</sub>-MMT/PCN@Pd nanocomposites, the characteristic (001) diffraction peaks become extremely broader and weaker, indicating almost disorderly alignment of the MMT silicate layers after the TiO<sub>2</sub> modification. Nevertheless, the basal space of 2.05 nm and interlayer spacing distance of 1.09 nm can be derived from the weak peak at 2θ of around 4.30°. According to the Lagaly's method [47–49], the bilayer arrangement of the CS chains (PCN precursor) and its derived PCN species occur in the pillared silicate interlayers.

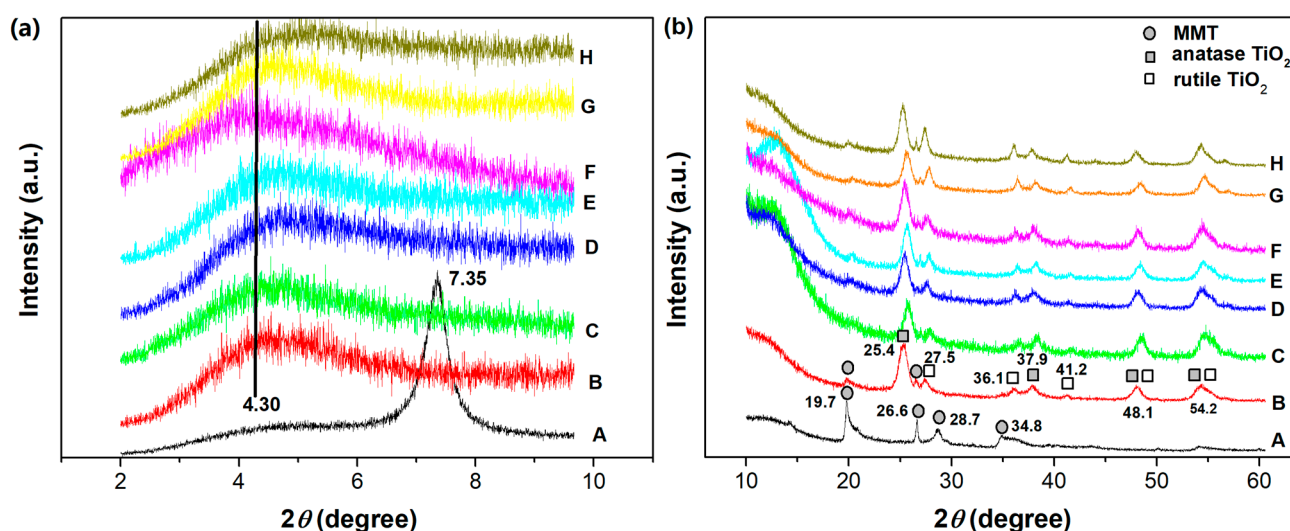


**Figure 1.** XRD patterns of the TiO<sub>2</sub>-MMT/PCN@Pd nanocomposites with 2θ small angle from 2 to 10° (a) and wide angle from 10 to 60° (b): A. MMT; B. TiO<sub>2</sub>-MMT; C. TiO<sub>2</sub>-MMT<sub>80</sub>/PCN<sub>20</sub>; D. TiO<sub>2</sub>-MMT<sub>80</sub>/PCN<sub>20</sub>@Pd<sup>2+</sup>; E. TiO<sub>2</sub>-MMT<sub>80</sub>/PCN<sub>20</sub>@Pd<sup>0</sup>; F. TiO<sub>2</sub>-MMT<sub>60</sub>/PCN<sub>40</sub>; G. TiO<sub>2</sub>-MMT<sub>60</sub>/PCN<sub>40</sub>@Pd<sup>2+</sup>; H. TiO<sub>2</sub>-MMT<sub>60</sub>/PCN<sub>40</sub>@Pd<sup>0</sup>.

As shown in Figure 1b, for Na-MMT, the diffraction peak at 2θ of 19.7° is related to the two-dimensional *hk* indices of (02) and (11), the diffraction peak at 2θ of 34.8° is related to the two-dimensional *hk* indices of (13) and (20), the diffraction peak at 26.6° is attributed

to quartz, and the diffraction peak at  $28.7^\circ$  is attributed to the silica impurity [50]. For  $\text{TiO}_2$ -MMT and all of the  $\text{TiO}_2$ -MMT/PCN@Pd nanocomposites, the  $hk$  reflection peaks at  $2\theta$  of about  $19.7^\circ$  are related to the two-dimensional MMT layers still present [51]. However, the relative intensity of the diffraction peak obviously decreases. This can be due to the formation of the crystalline  $\text{TiO}_2$  nanoparticles. As shown in Figure 1b, the new diffraction peaks at  $2\theta$  of about  $25.4^\circ$ ,  $27.5^\circ$ ,  $36.1^\circ$ ,  $37.9^\circ$ ,  $41.2^\circ$ ,  $48.1^\circ$ , and  $54.2^\circ$  are assigned to the  $\text{TiO}_2$  nanoparticles [52], indicating the presence of mainly anatase  $\text{TiO}_2$  together with some rutile  $\text{TiO}_2$  on the surface of the MMT layers after the calcination process. This phenomenon is quite different from that of the Al-pillared MMT [23,32,33,42], in which most of the intercalated polyhydroxy-Al cations are converted into stable  $\text{Al}_2\text{O}_3$  pillars instead of  $\text{Al}_2\text{O}_3$  nanoparticles dispersed on the surface of the MMT layer.

Further evidence of the successful  $\text{TiO}_2$ -pillaring modification can be found in the changes of the FTIR spectra of the starting MMT and the nanocomposites. As shown in Figure 2, after the  $\text{TiO}_2$  pillaring, carbonization and Pd-loading steps, the preservation of characteristic FTIR bands in the region of  $400\text{--}700\text{ cm}^{-1}$  ( $465\text{ cm}^{-1}$  assigned to Si-O-Si bending,  $527\text{ cm}^{-1}$  assigned to Al-O-Si bending) [53–56] is observed, indicating that the small building units of the MMT layer are still present. For pure MMT, the peak at  $915\text{ cm}^{-1}$  is assigned as the Si-OH vibration. After dehydroxylation in the high-temperature pillaring or carbonization process, the Si-OH vibration peak almost disappears and new peaks are found around  $930$  and  $945\text{ cm}^{-1}$ , which can be assigned to the Si-O-Ti vibration, confirming the molecular combination of the  $\text{TiO}_2$  species with the MMT frame.

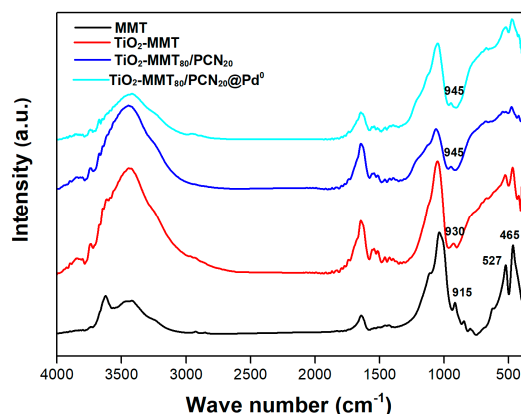


**Figure 2.** FTIR spectra of the MMT,  $\text{TiO}_2$ -MMT,  $\text{TiO}_2$ -MMT<sub>80</sub>/PCN<sub>20</sub> support, and  $\text{TiO}_2$ -MMT<sub>80</sub>/PCN<sub>20</sub>@Pd<sup>0</sup> nanocomposites.

On the one hand, the pillars successfully derived in the MMT interlayer space should originate from the molecular level of the  $\text{TiO}_2$  species, which are combined on the MMT layer at the molecular level by the Si-O-Ti bonds after the pillaring process (including the polycation precursor intercalation, hydrolysis, and calcination steps). On the other hand, as  $\text{TiO}_2$  also prefers to form nanoparticles with fine crystal structure after calcination at  $500^\circ\text{C}$ , some of the derived  $\text{TiO}_2$  nanoparticles with a larger size than the basal spacing of the pillared MMT might be sandwiched in the multilayer space of the pillared MMT. This results in some irregular stacking of the MMT layers, while the other derived  $\text{TiO}_2$  nanoparticles should be directly dispersed on the external surface of the MMT layers.

Due to the low loading content of Pd and its fine dispersion, the characteristic Pd<sup>0</sup> crystal diffraction peaks do not appear distinctly. Nevertheless, the Pd content within the catalyst can be supported using the ICP-AES and XPS determination. The percentage of Pd content within the  $\text{TiO}_2$ -MMT/PCN@Pd<sup>0</sup> nanocomposite is determined as about 2% using ICP-AES. Meanwhile, the binding energies of Pd<sub>3d</sub> are observed as  $335.6\text{ eV}$  (assigned to the Pd<sup>0</sup> species) and  $337.2\text{ eV}$  (assigned to the Pd<sup>2+</sup> species), confirming the presence of the Pd active species [57]. In addition to the Pd<sub>3d</sub>, the XPS spectra of C<sub>1s</sub>, O<sub>1s</sub>, and N<sub>1s</sub> are shown in Figure 3. For the XPS spectrum of C<sub>1s</sub> in PCN, it can be deconvoluted into three peaks at

284.4 eV (C atoms on C=C), 285.9 eV (C atoms on C-N and/or C-O), and 288.4 eV (C atoms on C=O), respectively. For the XPS spectrum of  $N_{1s}$  in PCN, it can be deconvoluted into four peaks at 399.2 eV (N atoms on pyridinic-N), 400.3 eV (N atoms on pyrrolic-N), 401.6 eV (N atoms on graphitic-N), and 403.0 eV (N atoms on N-O bonds), respectively. For the XPS spectrum of  $O_{1s}$ , it can be deconvoluted into two peaks at 530.5 eV (O atoms on C-O) and 532.1 eV (O atoms on C=O), respectively. Clearly, the derived N-containing PCN from CS successfully supported on the  $TiO_2$ -MMT is powerfully supported by the XPS results. The Raman shift of the prepared  $TiO_2$ -MMT<sub>60</sub>/PCN<sub>40</sub>@Pd<sup>0</sup> is illustrated in Figure 4. The peaks at about 1360  $cm^{-1}$  and 1590  $cm^{-1}$  are attributed to disordered and ordered graphite carbon species (the so-called D band and G band), respectively. The derived PCN is mainly composed of disordered carbon species as the  $I_D/I_G$  is found as 4.1.

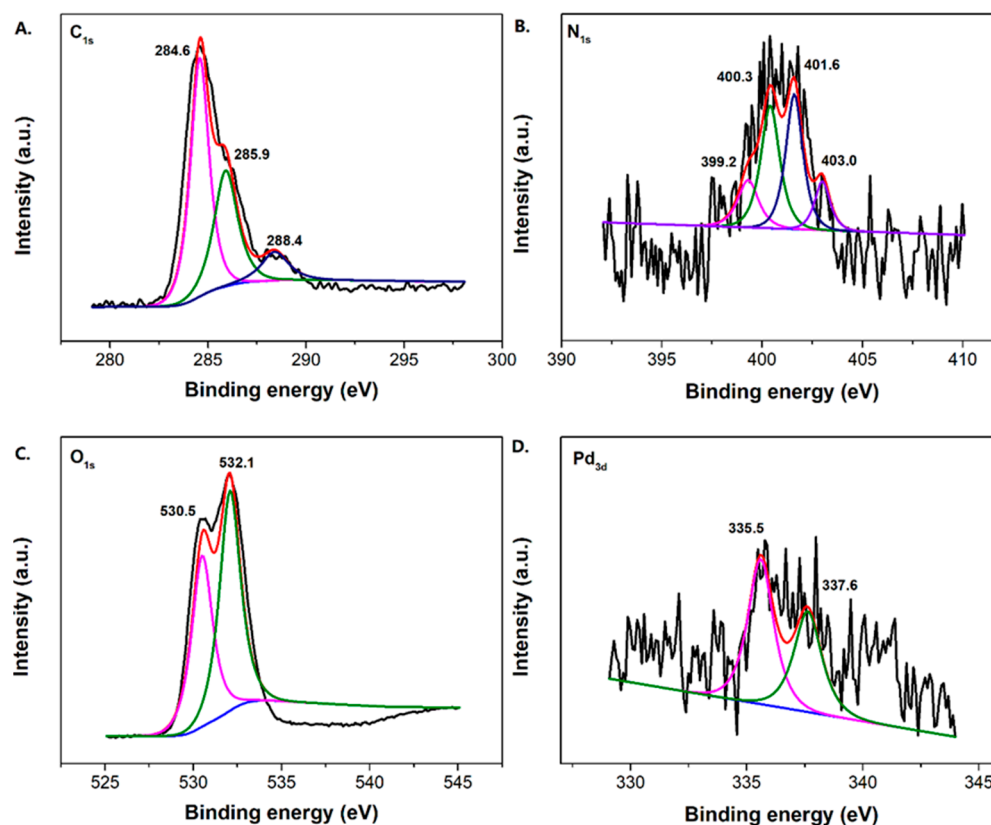


**Figure 3.** XPS spectrum of the  $C_{1s}$  (A),  $N_{1s}$  (B),  $O_{1s}$  (C), and  $Pd_{3d}$  (D) of the  $TiO_2$ -MMT<sub>60</sub>/PCN<sub>40</sub>@Pd<sup>0</sup> nanocomposites.

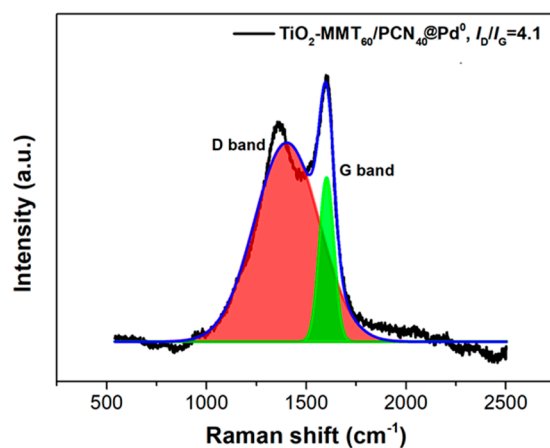


**Figure 4.** Raman shift of the  $TiO_2$ -MMT<sub>60</sub>/PCN<sub>40</sub>-Pd<sup>0</sup> nanocomposites.

The N<sub>2</sub> adsorption–desorption isotherms and corresponding pore size distribution of the starting Na-MMT, TiO<sub>2</sub>-MMT, and TiO<sub>2</sub>-MMT/PCN@Pd nanocomposites are shown in Figure 5. Based on the isotherms, the extracted BET surface area ( $S_{\text{BET}}$ ), micropore area ( $A_{\text{mic}}$ ), and total pore volume ( $V_{\text{tot}}$ ) are listed in Table 1. All of the samples show distinct hysteresis loops at a higher  $P/P_0$  of 0.4 and considerable adsorption amounts at a low relative pressure, suggesting type IV isotherms with fairly good adsorption capacity. For Na-MMT, the hysteresis loops are assigned to the typical H<sub>3</sub> type, implying poor mesopores. For the TiO<sub>2</sub>-MMT and TiO<sub>2</sub>-MMT/PCN@Pd nanocomposites, all of the hysteresis loops are assigned to the typical H<sub>4</sub> type, implying rich, narrow, and slit-like mesopores. The pore size distribution peaks of TiO<sub>2</sub>-MMT are located at about 4 nm (minor peak) and 10 nm (major peak). This suggests that TiO<sub>2</sub> modification leads to the effective formation of numerous mesoporous layered structures. After hybridizing with PCN and the Pd<sup>2+</sup> species, the pore size distribution peaks of TiO<sub>2</sub>-MMT/PCN show little shift, indicating that the introduction of these species has limited effects on the mesopore size of the TiO<sub>2</sub>-MMT matrix. However, both in the case of TiO<sub>2</sub>-MMT<sub>80</sub>/PCN<sub>20</sub>@Pd<sup>0</sup> and TiO<sub>2</sub>-MMT<sub>60</sub>/PCN<sub>40</sub>@Pd<sup>0</sup>, the pore distribution peaks become obviously broader in the range of 10–16 nm. The increase in the larger-sized mesopores is ascribed to the generation of numerous disordered mesopores due to the reduction in the Pd<sup>2+</sup> species to Pd<sup>0</sup> nanoparticles. The  $S_{\text{BET}}$  of TiO<sub>2</sub>-MMT (161.1 m<sup>2</sup>/g) is about 13.8 times that of the starting Na-MMT (11.6 m<sup>2</sup>/g). The  $V_{\text{tot}}$  of TiO<sub>2</sub>-MMT (0.37 cm<sup>3</sup>/g) is about 9.2 times that of the starting Na-MMT (0.04 cm<sup>3</sup>/g). This is closely related to the induction of a large number of new stable porous structures after TiO<sub>2</sub> pillaring, which is in good agreement with the XRD results. However, after the loading of the PCN and the Pd species, it is observed that the  $S_{\text{BET}}$  and  $V_{\text{tot}}$  show a reasonable decrease. For the TiO<sub>2</sub>-MMT<sub>80</sub>/PCN<sub>20</sub>@Pd<sup>0</sup> series,  $S_{\text{BET}}$  decreases to 137.3 m<sup>2</sup>·g<sup>−1</sup> (TiO<sub>2</sub>-MMT<sub>80</sub>/PCN<sub>20</sub>), 114.9 m<sup>2</sup>·g<sup>−1</sup> (TiO<sub>2</sub>-MMT<sub>80</sub>/PCN<sub>20</sub>@Pd<sup>2+</sup>), and 108.9 m<sup>2</sup>·g<sup>−1</sup> (TiO<sub>2</sub>-MMT<sub>80</sub>/PCN<sub>20</sub>@Pd<sup>0</sup>), respectively;  $V_{\text{tot}}$  shows a little decrease to 0.37 cm<sup>3</sup>/g (TiO<sub>2</sub>-MMT<sub>80</sub>/PCN<sub>20</sub>), 0.36 cm<sup>3</sup>/g (TiO<sub>2</sub>-MMT<sub>80</sub>/PCN<sub>20</sub>@Pd<sup>2+</sup>), and 0.27 cm<sup>3</sup>/g (TiO<sub>2</sub>-MMT<sub>80</sub>/PCN<sub>20</sub>@Pd<sup>0</sup>), respectively. For the TiO<sub>2</sub>-MMT<sub>60</sub>/PCN<sub>40</sub>@Pd<sup>0</sup> series,  $S_{\text{BET}}$  decreases to 124.2 m<sup>2</sup>·g<sup>−1</sup> (TiO<sub>2</sub>-MMT<sub>60</sub>/PCN<sub>40</sub>), 121.1 m<sup>2</sup>·g<sup>−1</sup> (TiO<sub>2</sub>-MMT<sub>60</sub>/PCN<sub>40</sub>@Pd<sup>2+</sup>), and 89.6 m<sup>2</sup>·g<sup>−1</sup> (TiO<sub>2</sub>-MMT<sub>60</sub>/PCN<sub>40</sub>@Pd<sup>0</sup>), respectively.  $V_{\text{tot}}$  shows a little decrease to 0.33 cm<sup>3</sup>/g (TiO<sub>2</sub>-MMT<sub>60</sub>/PCN<sub>40</sub>), 0.30 cm<sup>3</sup>/g (TiO<sub>2</sub>-MMT<sub>60</sub>/PCN<sub>40</sub>@Pd<sup>2+</sup>), and 0.27 cm<sup>3</sup>/g (TiO<sub>2</sub>-MMT<sub>60</sub>/PCN<sub>40</sub>@Pd<sup>0</sup>), respectively. Nevertheless, the adsorption capacity and porosity of such novel TiO<sub>2</sub>-MMT/PCN@Pd<sup>0</sup> is superior to the recently prepared adsorbents or heterogeneous catalysts using TiO<sub>2</sub>-pillared MMT or MMT/PCN composites as a matrix [35–40]. As confirmed in the adsorption tests for the rhodamine B dye at room temperature (as shown in Figure 6), both TiO<sub>2</sub>-MMT<sub>80</sub>/PCN<sub>20</sub>@Pd<sup>0</sup> and TiO<sub>2</sub>-MMT<sub>60</sub>/PCN<sub>40</sub>@Pd<sup>0</sup> show fairly good adsorption removal efficiency for the dye molecules (only 20 min reaching the equilibrium adsorption removal). Obviously, the former (92.1%) is better than the latter (79.6%). This might be due to the higher surface area of TiO<sub>2</sub>-MMT<sub>80</sub>/PCN<sub>20</sub>@Pd<sup>0</sup> than TiO<sub>2</sub>-MMT<sub>60</sub>/PCN<sub>40</sub>@Pd<sup>0</sup>. The highly porous structure and high surface area performance should be in favor of excellent catalytic performance of the resultant nanocomposites.

**Table 1.** Structural parameters of TiO<sub>2</sub>-MMT/PCN@Pd nanocomposites extracted from the isotherms in Figure 5.

Sample	$S_{\text{BET}}$ (m <sup>2</sup> /g)	$A_{\text{mic}}$ (m <sup>2</sup> /g)	$V_{\text{tot}}$ (cm <sup>3</sup> /g)
MMT	11.6 ± 2.1	2.8 ± 0.5	0.04 ± 0.01
TiO <sub>2</sub> -MMT	161.1 ± 13.6	49.5 ± 6.7	0.37 ± 0.01
TiO <sub>2</sub> -MMT <sub>80</sub> /PCN <sub>20</sub>	137.3 ± 12.9	42.5 ± 7.2	0.37 ± 0.01
TiO <sub>2</sub> -MMT <sub>80</sub> /PCN <sub>20</sub> @Pd <sup>2+</sup>	114.9 ± 11.5	32.7 ± 5.8	0.36 ± 0.01
TiO <sub>2</sub> -MMT <sub>80</sub> /PCN <sub>20</sub> @Pd <sup>0</sup>	108.9 ± 10.6	31.2 ± 5.7	0.27 ± 0.01
TiO <sub>2</sub> -MMT <sub>60</sub> /PCN <sub>40</sub>	124.2 ± 11.2	35.3 ± 6.2	0.33 ± 0.01
TiO <sub>2</sub> -MMT <sub>60</sub> /PCN <sub>40</sub> @Pd <sup>2+</sup>	121.1 ± 12.3	38.7 ± 6.9	0.30 ± 0.01
TiO <sub>2</sub> -MMT <sub>60</sub> /PCN <sub>40</sub> @Pd <sup>0</sup>	89.6 ± 10.6	15.7 ± 7.1	0.35 ± 0.01

$S_{\text{BET}}$ : specific surface area, using the Brunauer–Emmet–Teller method;  $A_{\text{mic}}$ : micropore area obtained using the  $t$ -Polt method;  $V_{\text{tot}}$ : total volume of pores, the N<sub>2</sub> quantity adsorbed at a relative pressure of  $P/P_0 = 0.99$ .

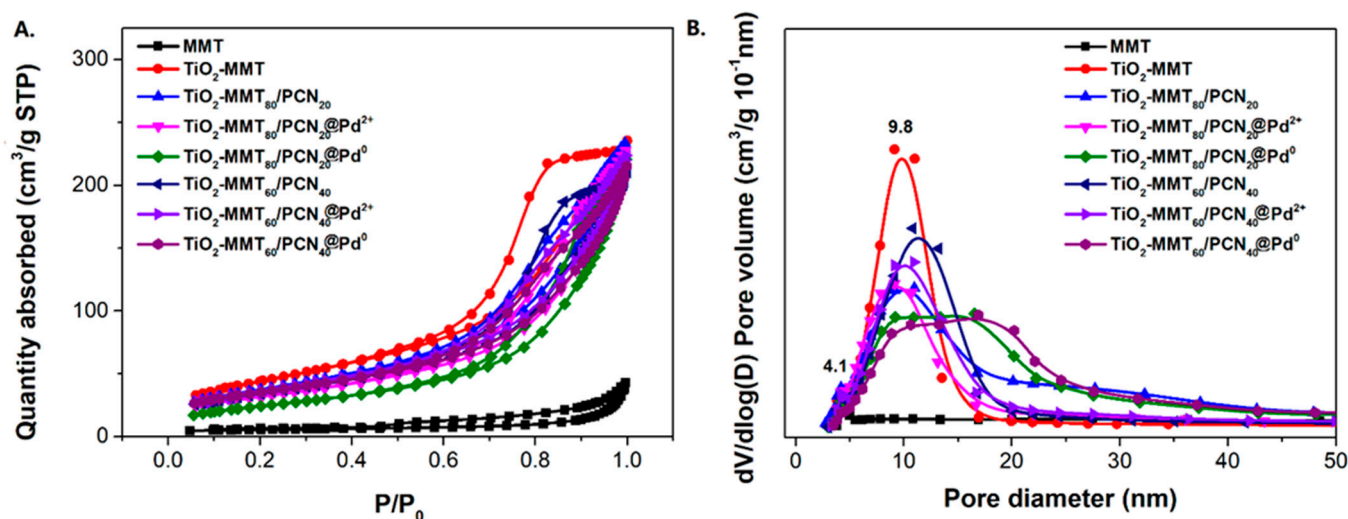


**Figure 5.**  $N_2$  adsorption/desorption isotherms (A) and corresponding pore size distribution (B) of the  $\text{TiO}_2$ -MMT/PCN@Pd nanocomposites.

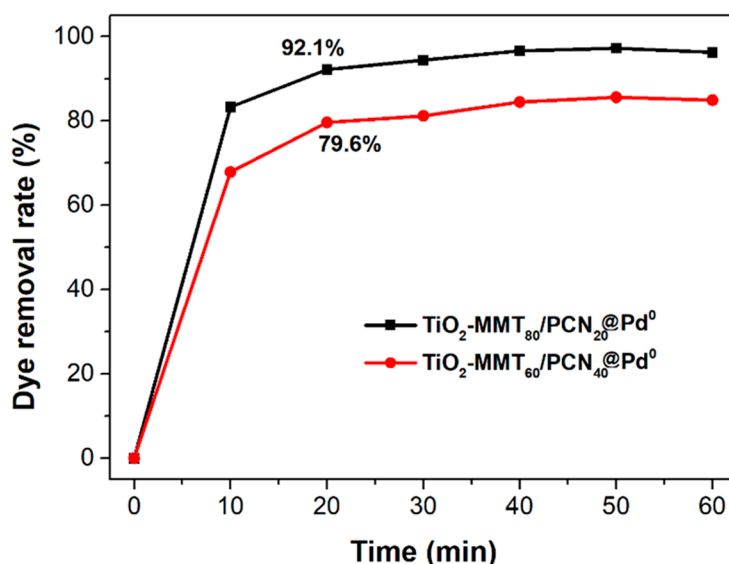


**Figure 6.** Adsorption removal rate of rhodamine B from the aqueous solution using the  $\text{TiO}_2$ -MMT<sub>80</sub>/PCN<sub>20</sub>@Pd<sup>0</sup> and  $\text{TiO}_2$ -MMT<sub>60</sub>/PCN<sub>40</sub>@Pd<sup>0</sup> nanocomposites.

The HRTEM-EDX images of the starting Na-MMT,  $\text{TiO}_2$ -MMT/PCN support and  $\text{TiO}_2$ -MMT/PCN@Pd nanocomposites are shown in Figure 7. The starting MMT exhibits a layered structure with a regular stacking and closing interlayer distance (Figure 7A). For  $\text{TiO}_2$ -MMT, the loaded  $\text{TiO}_2$  exist in three forms. Firstly, increasing of the interlayer distance and contrast is observed, indicating successful pillaring of the  $\text{TiO}_2$  species. However, the  $\text{TiO}_2$  pillars seem difficult to identify using HRTEM, which can be due to the molecular level combing of the  $\text{TiO}_2$  species with the MMT framework of the Si-O-Ti bonds. Similar phenomenon are also reported in other studies on pillared MMT characterized with TEM [58–60]. Secondly, it is observed (as marked with a blue rectangle) that some  $\text{TiO}_2$  nanoparticles sized about 5 nm are clipped in multilayer spaces of the MMT, causing an obvious disordered stacking of the MMT layers. Thirdly, many of the other visible  $\text{TiO}_2$  nanoparticles disperse directly on the external surface and/or edge of the MMT layers. After immobilization of the Pd species, it is observed that some additional nanoparticles (with sizes below 2 nm, as marked with red circles) are clipped in the space of the adjacent MMT layers, which can be attributed to the Pd<sup>0</sup> species. Unfortunately, for the low contrast,

the successful loading of the PCN species is difficult to identify with the HRTEM images. Nevertheless, with the element mapping and weight ratio results from the HRTEM-EDX, the successful loading of the PCN and Pd species is further confirmed. Based on the HRTEM-EDX results, the actual chemical composition of the  $\text{TiO}_2\text{-MMT}_{60}/\text{PCN}_{40}@Pd^0$  may be estimated as 47% of MMT, 41% of  $\text{TiO}_2$ , 11% of PCN, and 1% of Pd, respectively. As shown in Figure S1, the success incorporation of the PCN and Pd species can also be powerfully supported by the element's composition of the  $\text{TiO}_2\text{-MMT}_{60}/\text{PCN}_{40}@Pd^0$  using SEM-EDX. Clearly, the HRTEM-EDX results are consistent with the XRD, FTIR, and  $\text{N}_2$  adsorption–desorption results.

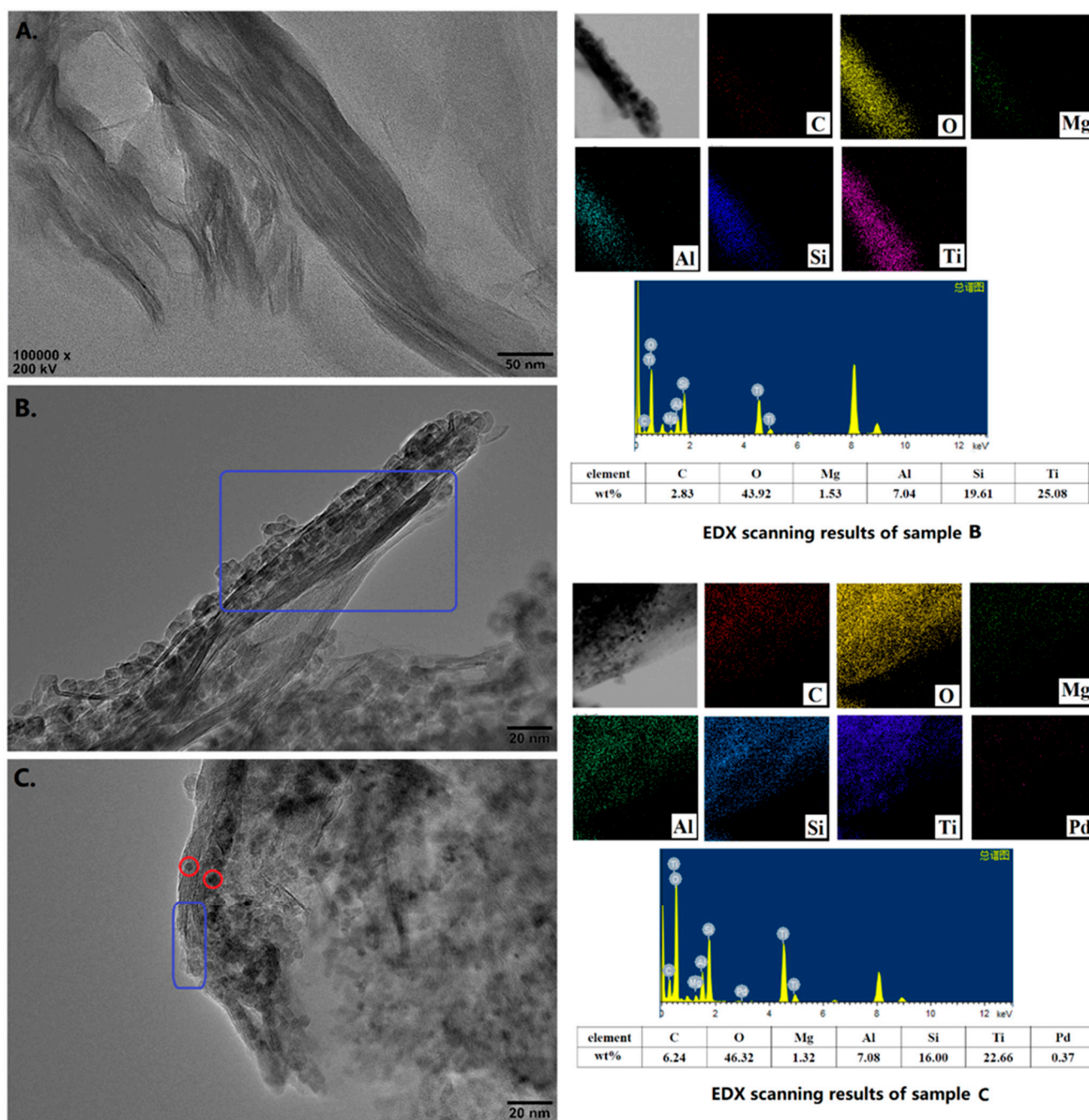
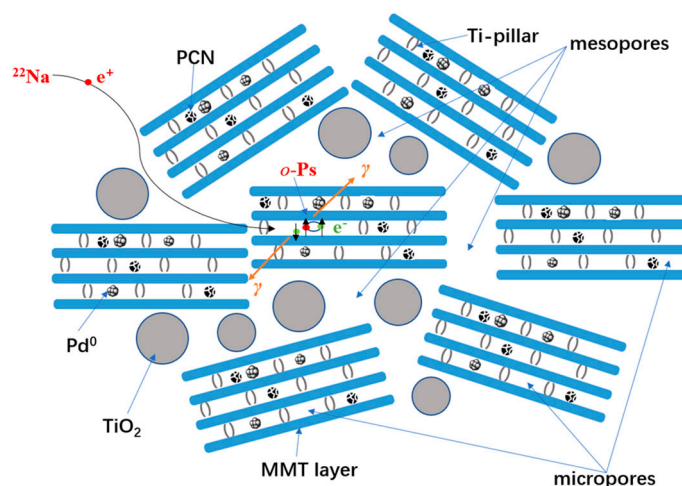


**Figure 7.** HRTEM images and element mapping results of the starting MMT (A),  $\text{TiO}_2\text{-MMT}_{60}/\text{PCN}_{40}$  (B), and  $\text{TiO}_2\text{-MMT}_{60}/\text{PCN}_{40}@Pd^0$  nanocomposite (C).

## 2.2. Positron Annihilation Characteristics of the Catalytic Nanocomposites

According to the microstructure characterization results above, the textile structure of the nanocomposite can be illustrated in Scheme 1. The mesoporous structure (using the N<sub>2</sub> adsorption–desorption isotherms and adsorption-removal test), interlayer spacing (using XRD), morphologies (using HRTEM), and compositions (using HRTEM-EDX, Raman spectroscopy, FTIR) are successfully revealed. However, the sub-nano level microstructure, such as the molecular packing information of the derived TiO<sub>2</sub> pillars, PCN, and active Pd species inside the TiO<sub>2</sub>-modified MMT layer space still lacks essential evidence. Positron annihilation lifetime spectroscopy (PALS) has recently been proven as one of the most highly sensitive methods to detect microstructure information at the sub-nano level [61–65]. In the interlayer space with low electron density, in addition to free positron annihilation, some of the thermalized positrons can be trapped with electrons to form a bound state called positronium (Ps), and then annihilate. Ps has two states, *o*-Ps (spin parallel) and *p*-Ps (spin antiparallel), depending on the spin orientations of the positrons and bound electrons. In a vacuum, the intrinsic lifetimes of *p*-Ps and *o*-Ps are 0.125 ns and 142 ns, respectively. In molecular solids, *o*-Ps will form interactions with the electrons in the surrounding medium and undergo pick-up annihilation, resulting in a reduction in the lifetime of 1 to several ns. Using a suitable quantum mechanical model [66,67], the *o*-Ps lifetime is correlated to the microdefect size. It can then be used as a sensitive probe to detect the local microdefect structure.



**Scheme 1.** Schematic presentation of *o*-Ps pick-off annihilation in the interlayer spaces of the TiO<sub>2</sub>-MMT<sub>60</sub>/PCN<sub>40</sub>@Pd<sup>0</sup> nanocomposites.

In such TiO<sub>2</sub>-MMT/PCN@Pd nanocomposite systems, as shown in Scheme 1, *o*-Ps annihilation should mainly occur in the molecule-stacking gaps in all of the involved molecular substrates in the interlayer space of the MMT with low electron density, such as the PCN molecules, Pd species, TiO<sub>2</sub> pillars, and MMT layers. Using the quantum mechanical model in Equation (1) [68,69], the width of the cuboidal defects size can be estimated, where  $\tau_3$  refers to the longest lifetime,  $l$  refers to the width of the cuboidal defects size, and  $\Delta l$  (=0.17 nm) refers to the thickness of the fitted empirical electron layer. Therefore, *o*-Ps can be used as a highly sensitive probe to detect the molecule packing and interfacial interactions in the interlayer space of the MMT layers. The microdefects fraction,  $f$ , i.e., a combination of *o*-Ps intensity  $I_3$  with microdefects volume ( $V = l^3$ ), can be calculated according to Equation (2), where  $C$  is a constant. To simplify, the apparent microdefects fraction ( $f_{app}$ ) is often used to determine the variation trends.

$$\tau_3 = 0.5 \left[ 1 - \left( \frac{l}{l + 2\Delta l} + \frac{1}{\pi} \sin \frac{\pi l}{l + 2\Delta l} \right) \right]^{-1} \quad (1)$$

$$f = CVI_3 \text{ or } f_{\text{app}} = VI_3 \quad (2)$$

As shown in Table 2, the positron annihilation spectra of the nanocomposites are fitted well in the three-lifetime fitting with the LT-9 program. For all of the samples, the first lifetime component of  $\tau_1$  and its intensity of  $I_1$  can be attributed to a combination of *p*-Ps annihilation and free positron annihilation. The second lifetime component of  $\tau_2$  and its intensity of  $I_2$  can be attributed to a combination of free positron annihilation and some trapped positron annihilation in the microdefects of the crystalline MMT layers. The third long lifetime component of  $\tau_3$  and its intensity of  $I_3$  can be attributed to the *o*-Ps pick-off annihilation in the interlayer spaces of the TiO<sub>2</sub>-MMT<sub>60</sub>/PCN<sub>40</sub>@Pd<sup>0</sup> nanocomposites as illustrated in Scheme 1. In the confined nanospace between the neighboring layers, the *o*-Ps will be mainly trapped in the molecular packing gaps of the involved substrates, such as the MMT layer, PCN species, Pd species, and TiO<sub>2</sub> species. Using the cuboidal microdefects model in Equation (1), the size of the microdefects inside the interlayer space can be calculated. The microdefects size (*l*) inside the interlayer space of pure MMT can be calculated as 0.290 nm. After TiO<sub>2</sub> pillaring, modification, and further PCN derivation, the microdefects size of *l* increases to 0.307 nm (TiO<sub>2</sub>-MMT) and 0.311 nm (TiO<sub>2</sub>-MMT<sub>60</sub>/PCN<sub>40</sub>). This increase in size can be related to the increase in interlayer space caused by the effective high-temperature process during the TiO<sub>2</sub> pillaring and carbonization steps. After Pd<sup>2+</sup> immobilization and further reduction in the nano Pd<sup>0</sup> species, the microdefect size of *l* decreases to 0.308 nm (TiO<sub>2</sub>-MMT<sub>60</sub>/PCN<sub>40</sub>@Pd<sup>2+</sup>) and 0.299 nm (TiO<sub>2</sub>-MMT<sub>60</sub>/PCN<sub>40</sub>@Pd<sup>0</sup>), which confirms that the interlayer space becomes more crowded after the Pd species are successfully incorporated into the interlayer space of the modified MMT. Moreover, it is observed that the both  $I_3$  and  $f_{\text{app}}$  of the TiO<sub>2</sub>-MMT<sub>60</sub>/PCN<sub>40</sub>@Pd nanocomposites are higher than the starting MMT, TiO<sub>2</sub>-MMT, and TiO<sub>2</sub>-MMT<sub>60</sub>/PCN<sub>40</sub> supports. This means that the nanocomposite still has high microdefect features though the interlayer spaces is more crowded. As microdefects can be used as active sites for catalytic reactions, a high comprehensive catalytic performance of the TiO<sub>2</sub>-MMT<sub>60</sub>/PCN<sub>40</sub>@Pd nanocomposites is expected.

**Table 2.** Variation in microdefect results obtained from PALS spectra of the TiO<sub>2</sub>-MMT/PCN@Pd nanocomposites with three-lifetime fitting. Experimental errors are given in parentheses in terms of uncertainty of the last meaningful digit.

Sample	$\tau_1$ (ns)	$I_1$ (%)	$\tau_2$ (ns)	$I_2$ (%)	$\tau_3$ (ns)	$I_3$ (%)	<i>l</i> (nm)	$f_{\text{app}}$ (%)
MMT	0.247 (2)	57.4 (7)	0.486 (4)	40.0 (6)	2.238 (3)	2.6 (2)	0.290	0.063
TiO <sub>2</sub> -MMT	0.239 (2)	56.1 (7)	0.438 (6)	41.9 (8)	2.398 (3)	1.9 (2)	0.307	0.055
TiO <sub>2</sub> -MMT <sub>60</sub> /PCN <sub>40</sub>	0.243 (2)	56.8 (7)	0.433 (6)	41.3 (9)	2.440 (4)	1.9 (2)	0.311	0.057
TiO <sub>2</sub> -MMT <sub>60</sub> /PCN <sub>40</sub> @Pd <sup>2+</sup>	0.222 (2)	51.2 (7)	0.434 (6)	41.3 (8)	2.409 (3)	3.5 (3)	0.308	0.102
TiO <sub>2</sub> -MMT <sub>60</sub> /PCN <sub>40</sub> @Pd <sup>0</sup>	0.224 (2)	57.4 (7)	0.421 (6)	39.6 (8)	2.331 (4)	3.0 (2)	0.299	0.080

### 2.3. Performances of the Catalytic Nanocomposites Applied in Sonogashira Reactions

The Sonogashira reaction, usually referring to the cross-coupling reaction of terminal alkyne with aryl halides, is an extremely valuable type of reaction to form C-C (sp-sp<sub>2</sub>) bonds [70–72]. It has been broadly used in the field of synthesis of functional molecules of natural products, biological active features, pharmaceuticals, heterocycles, conducting polymers, and liquid polymer substrates, etc. Firstly, the catalytic performances of the TiO<sub>2</sub>-MMT/PCN@Pd nanocomposites are evaluated with a typical model Sonogashira reaction of iodo benzene and phenyl acetylene. The Pd<sup>0</sup> species supported on TiO<sub>2</sub>, PCN, TiO<sub>2</sub>/PCN, MMT/PCN, and TiO<sub>2</sub>-MMT are prepared and their N<sub>2</sub> adsorption performances are shown in Figure S2 and Table S1. As shown in Table S2, the model Sonogashira reaction is found to be difficult to perform without any Pd catalyst. However, with the presence of different Pd catalysts, such as TiO<sub>2</sub>@Pd<sup>0</sup>, PCN@Pd<sup>0</sup>, TiO<sub>2</sub>/PCN@Pd<sup>0</sup>, MMT/PCN@Pd<sup>0</sup>, and TiO<sub>2</sub>-MMT@Pd<sup>0</sup>, the reaction can be fairly well catalyzed with good yields (Figure S3A). As shown in Figure 8A, for each reaction time interval, it is found that

the reaction yields catalyzed by  $\text{TiO}_2\text{-MMT}_{80}/\text{PCN}_{20}@\text{Pd}^0$  are higher than that catalyzed by  $\text{TiO}_2\text{-MMT}_{60}/\text{PCN}_{40}@\text{Pd}^0$ , which should be mainly attributed to its higher adsorption capability [73,74]. The recyclability of the catalysts is further evaluated as applied in the model reaction. At each reaction time interval, hardly any improvements of the yields are observed after a hot filtration out of both catalysts, confirming the high heterogeneity. As shown in Figure 8B, for maintaining the yield higher than 70%,  $\text{TiO}_2\text{-MMT}_{80}/\text{PCN}_{20}@\text{Pd}^0$  and  $\text{TiO}_2\text{-MMT}_{60}/\text{PCN}_{40}@\text{Pd}^0$  can recycle for 16 runs and 19 runs, respectively. Obviously, as compared with the recyclable runs of  $\text{TiO}_2\text{-Pd}^0$  (six runs),  $\text{PCN-Pd}^0$  (ten runs),  $\text{TiO}_2/\text{PCN-Pd}^0$  (eleven runs),  $\text{MMT}/\text{PCN-Pd}^0$  (eight runs), and  $\text{TiO}_2\text{-MMT-Pd}^0$  (six runs) (as shown in Figure S3B), a combination of the PCN, MMT, and  $\text{TiO}_2$  into a composite support Pd metal catalyst shows effective synergism improvements in the recyclability of the resultant  $\text{TiO}_2\text{-MMT}/\text{PCN}@\text{Pd}^0$  catalytic nanocomposites. Moreover, as shown in Figure 8C and Table S3,  $\text{TiO}_2\text{-MMT}/\text{PCN}@\text{Pd}$  shows higher stability than most of the recently developed Pd heterogeneous catalysts for Sonogashira reactions with similar reaction conditions, including Pd loaded on modified  $\text{TiO}_2$  ( $\text{h-Fe}_3\text{O}_4@\text{TiO}_2\text{-NH}_2/\text{Pd}$  or  $(\text{TiO}_2@\text{Pd}(\text{II}))[\text{PATA-NH}_2]$ ) [75,76], MMT ( $\text{K10}@\text{Pd}(\text{II})\text{APTES}$  or  $\text{MMT}/\text{CS}@\text{Pd}$ , Cu) [77,78], or carbon-based supports ( $\text{CHT}@\text{Pd}$  or  $\text{Hal-pDA-NPC}@\text{Pd}$ ) [79,80]. The excellent chelation, stability, and adsorption of  $\text{TiO}_2$ , MMT, and PCN have been well combined into a composite material, resulting in an effectively synergetic performance improvement in the case of the  $\text{TiO}_2\text{-MMT}/\text{PCN}@\text{Pd}$  catalyst. The higher stability (three more recyclable runs) of  $\text{TiO}_2\text{-MMT}_{60}/\text{PCN}_{40}@\text{Pd}^0$  than  $\text{TiO}_2\text{-MMT}_{80}/\text{PCN}_{20}@\text{Pd}^0$  may be attributed to its higher content of the PCN, which has reasonably stronger chelation with the Pd species as compared with inorganic  $\text{TiO}_2$  or MMT. Hence, further evaluation of the catalyst performance was mainly focused on the case of  $\text{TiO}_2\text{-MMT}_{60}/\text{PCN}_{40}@\text{Pd}^0$  with a higher content of PCN. As tracked using the ICP-AES assay, about 93% and 81% of the Pd species retained in the recovered  $\text{TiO}_2\text{-MMT}_{60}/\text{PCN}_{40}@\text{Pd}^0$  for five runs and ten runs, respectively. To clarify the reason for the Pd leaching, the recovered catalyst was further characterized with PALS.

As shown in Figure 8D, distinct differences are observed for the  $\text{TiO}_2\text{-MMT}_{60}/\text{PCN}_{40}@\text{Pd}^0$  after recycled for different times. As compared with the fresh  $\text{TiO}_2\text{-MMT}_{60}/\text{PCN}_{40}@\text{Pd}^0$  nanocomposite, many more counts of *o*-Ps annihilations with a longer lifetime ( $>2.5$  ns) are observed for the PALS spectra of the recycled nanocomposites. This indicates that the recycled nanocomposites may contain more than one long-lifetime component as the usual molecular solids. Therefore, the positron annihilation spectra of the recycled nanocomposites have been refitted in four-lifetime rather than the usual three-lifetime fitting. The PALS spectrum of fresh  $\text{TiO}_2\text{-MMT}_{60}/\text{PCN}_{40}@\text{Pd}^0$  catalyst has been also fitted in the four-lifetime component for comparison. As shown in Table 3, for the spectrum of fresh  $\text{TiO}_2\text{-MMT}_{60}/\text{PCN}_{40}@\text{Pd}^0$  nanocomposite, we obtained  $\tau_1 = 0.249$  ns,  $\tau_2 = 0.372$  ns,  $\tau_3 = 0.472$  ns, and  $\tau_4 = 2.11$  ns with the relative intensities  $I_1 = 71.3\%$ ,  $I_2 = 8.8\%$ ,  $I_3 = 18.0\%$ , and  $I_4 = 1.9\%$ , exhibiting three short-lifetime components ( $<0.5$  ns) and one long-lifetime component ( $>1$  ns). The first two short-lifetime components of  $\tau_1$  and  $\tau_2$  can be attributed to the *p*-Ps decay and free positron annihilations. The third short-lifetime component of  $\tau_3$  can be attributed to free positron annihilations and some trapped positron annihilations in the microdefects of the MMT crystalline layer and the  $\text{TiO}_2$  nanoparticle crystals. The long-lifetime component of  $\tau_4$  can be attributed to *o*-Ps pick-off annihilations in the molecules stacking gaps of all of the involved molecular substrates, such as the PCN molecules, Pd species,  $\text{TiO}_2$  nanoparticles, and MMT layers. The mean microdefects size  $l$  (from  $\tau_4$ ) of the fresh  $\text{TiO}_2\text{-MMT}_{60}/\text{PCN}_{40}@\text{Pd}^0$  is estimated as 0.277 nm. Clearly, this size value is even smaller than the microdefects size  $l$  of 0.299 nm that is obtained from the three-lifetime fitting (as shown in Table 2). This indicates that the PCN and Pd species are tightly engaged in the nanospace of the  $\text{TiO}_2$ -pillared MMT layers and three-lifetime fitting is more reasonable than four-lifetime fitting for fresh  $\text{TiO}_2\text{-MMT}_{60}/\text{PCN}_{40}@\text{Pd}^0$  nanocomposites.

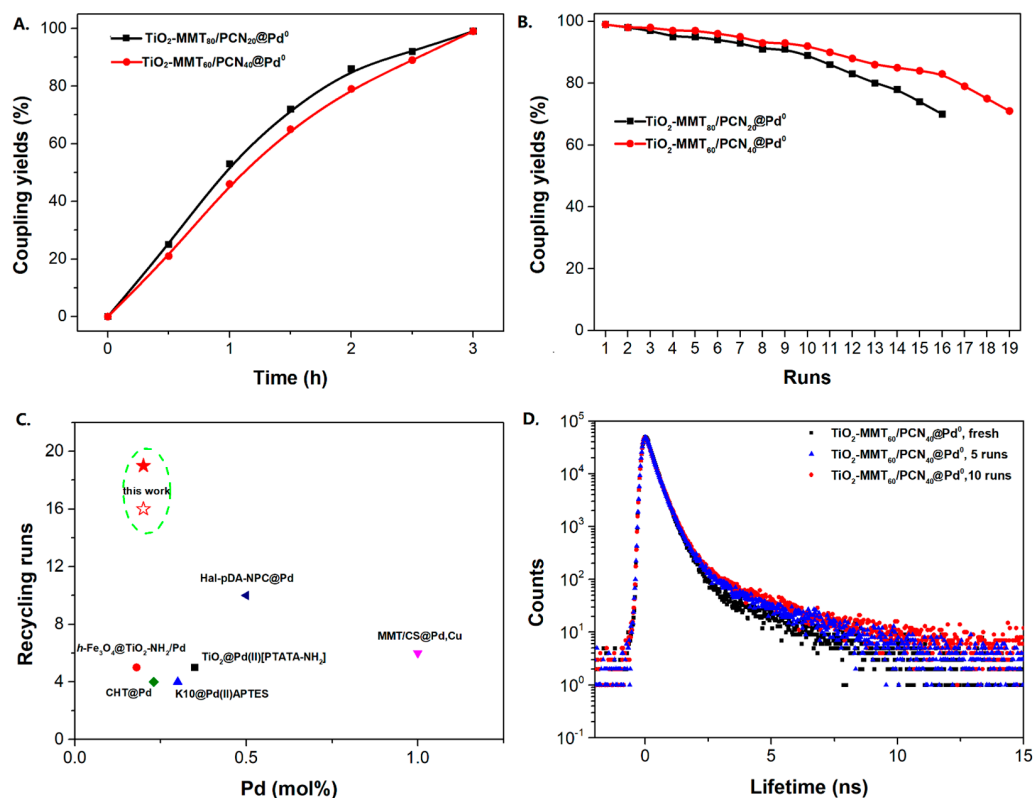


**Figure 8.** Recycling stabilities of the  $\text{TiO}_2\text{-MMT}/\text{PCN}@Pd^0$  nanocomposites: (A) Coupling yields vs time; (B) Coupling yields vs recycling runs; (C) Comparing with recently developed catalysts; (D) Microstructure changes of the catalyst tracked using PALS determination.

**Table 3.** Variation in microdefect results obtained from PALS spectra of the recovered  $\text{TiO}_2\text{-MMT}_{60}/\text{PCN}_{40}@Pd^0$  nanocomposites with four-lifetime fitting. Experimental errors are provided in parentheses in term of uncertainty of the last meaningful digit.

Sample	$\tau_1$ (ns)	$I_1$ (%)	$\tau_2$ (ns)	$I_2$ (%)	$\tau_3$ (ns)	$I_3$ (%)	$\tau_4$ (ns)	$I_4$ (%)	$l$ (nm)
$C_f$	0.249 (2)	71.3 (9)	0.372 (4)	8.8 (6)	0.472 (4)	18.0 (5)	2.11 (6)	1.9 (2)	0.277
$C_5$	0.216 (2)	54.0 (8)	0.407 (4)	42.6 (7)	2.13 (5)	3.1 (3)	7.20 (8)	0.3 (1)	0.279, 0.616
$C_{10}$	0.211 (2)	50.3 (8)	0.413 (4)	45.5 (7)	2.08 (5)	3.6 (3)	8.7 (8)	0.6 (1)	0.274, 0.681

$C_f$ :  $\text{TiO}_2\text{-MMT}_{60}/\text{PCN}_{40}@Pd^0$ , fresh;  $C_5$ :  $\text{TiO}_2\text{-MMT}_{60}/\text{PCN}_{40}@Pd^0$ , five runs;  $C_{10}$ :  $\text{TiO}_2\text{-MMT}_{60}/\text{PCN}_{40}@Pd^0$ , ten runs.

Unlike the fresh catalyst, after recycled for five runs or ten runs, two long-lifetime components ( $>1$  ns) of  $\tau_3$  and  $\tau_4$  are observed. For the recycled  $\text{TiO}_2\text{-MMT}_{60}/\text{PCN}_{40}@Pd^0$  catalytic nanocomposite recycled for five runs, besides the first long-lifetime component of  $\tau_3 = 2.13$  ns (close to the long-lifetime of  $\tau_4$  of the fresh catalytic nanocomposite), the second long-lifetime of  $\tau_4$  is observed as 7.2 ns (with the relative intensities of  $I_4 = 0.26\%$ ). This indicates that *o*-Ps pick-off annihilations occur in other much larger-sized microdefects. The microdefect sizes of the five-runs recycled  $\text{TiO}_2\text{-MMT}_{60}/\text{PCN}_{40}@Pd^0$  catalyst are estimated as 0.279 nm and 0.616 nm. Similarly, for the recycled  $\text{TiO}_2\text{-MMT}_{60}/\text{PCN}_{40}@Pd^0$  catalyst recycled for ten runs, the microdefects sizes are estimated as 0.274 nm and 0.681 nm. This suggests that PALS is highly sensitive to the development of microdefects and provides direct evidence for the induction of some larger-sized microdefects during sequential recycling. Meanwhile, the relative intensities of *o*-Ps annihilation ( $I_3 + I_4$ ) of the five-runs recycled catalyst ( $I_3 + I_4 = 3.3\%$ ) and ten-runs recycled catalyst ( $I_3 + I_4 = 4.2\%$ ) are

obviously higher than that of fresh catalyst ( $I_4 = 1.9\%$ ), indicating that more microdefects form after the continuous recycling process. Although larger-sized microdefects have low intensities, some of them may provide leaching channels for load molecules, including active Pd species.

Moreover, the novel  $\text{TiO}_2\text{-MMT}_{60}/\text{PCN}_{40}@\text{Pd}^0$  nanocomposite can be successfully extended to a range of substituted aryl halides coupling with phenyl acetylenes. As shown in Table 4, the reactions of the aryl iodides substituted with electron-donating groups of  $-\text{CH}_3$  at ortho (entry 2), meta (entry 3), or para (entry 4) positions with phenylacetylene achieved excellent yields of 92–99%. Furthermore, the reactions of the aryl iodides substituted with electron-withdrawing groups of  $-\text{F}$ ,  $-\text{Br}$ , and  $-\text{Cl}$  at ortho (entry 5), meta (entry 6), or para (entry 7) positions with phenylacetylene achieved excellent yields of 93–99%. For the entries 8–12, the reactions of the substituted aryl bromides with phenyl acetylene can be still effectively catalyzed with the novel  $\text{TiO}_2\text{-MMT}_{60}/\text{PCN}_{40}\text{-Pd}^0$  nanocomposite with desirable yields of 59–72%. In addition, the novel catalysts can efficiently catalyze the large-sized reactants for the coupling of iodo naphthalene and iodo fluorene with phenyl acetylene (entry 13, 14), indicating the high feasibility of molecular size. Conclusively, the  $\text{TiO}_2\text{-MMT}_{60}/\text{PCN}_{40}@\text{Pd}^0$  nanocomposite developed in this study shows similarly high catalytic efficiency as compared with recently reported heterogeneous Pd catalysts for Sonogashira reactions with similar reaction conditions [23,75–80]. The good dispersion and tight loading of the Pd species in the highly porous, stable, and amphiphilic  $\text{TiO}_2$ -pillared MMT-supported PCN matrix is likely the main reason for this high catalytic efficiency.

**Table 4.** Catalytic performance of  $\text{TiO}_2\text{-MMT}_{60}/\text{PCN}_{40}@\text{Pd}^0$  nanocomposites applied in Sonogashira coupling reactions between aromatic halides and alkynes.

$\text{X}=\text{I}, \text{Br}$

Entry	Aromatic Halides	Alkynes	Yield (%) <sup>a</sup>
1			99
2			92
3			98
4			97
5			93
6			96

Table 4. Cont.

X=I, Br

Entry	Aromatic Halides	Alkynes	Yield (%) <sup>a</sup>
7			99
8			68
9			59
10			62
11			70
12			72
13			99
14			97

<sup>a</sup>: GC/MS yields.

### 3. Materials and Methods

**Materials:** G-105 type Na<sup>+</sup>-MMT clay from Nanocor Co., USA, with cationic exchange capacity of 145 meq/100 g, was used as the starting material. Chitosan (CS) from Zhejiang Aoxing Biotechnology Co., Ltd., viscosity molecular weight of  $1.2 \times 10^5$  and deacetylated degree of 95%, was used as the precursor of porous carbon (PCN). All of the chemical reagents and reactant molecules involved in Sonogashira reactions used in this study were of analytical grade without further purification.

**Preparations:** The TiO<sub>2</sub>-modified MMT was prepared using similar processes as in recent studies [39]. TiCl<sub>4</sub> was added dropwise into 2 mol/L HCl solution under mechanical stirring and ice–water (0 °C) bath. The mixture was then diluted to reach the concentration of 0.6 mol/L of H<sup>+</sup> and 0.82 mol/L of Ti<sup>4+</sup>, respectively. The pillaring solution was aged for 12 h at 25 °C prior to its use. The pillaring solution was added dropwise into 10 wt% Na<sup>+</sup>-MMT clay aqueous suspension, to reach the Ti<sup>4+</sup>/Na<sup>+</sup>-MMT clay ratio of 20 mmol/1 g. The mixed suspension was kept mechanically stirring for 6 h at 60 °C, and then it was centrifuged and washed with deionized water to neutral. After naturally drying, the mixture was calcined in a tubular muffle furnace (BTF-1600C, Anhui BEQ Equipment Technology Co., Ltd., Hefei, China) for 3 h at a temperature of 500 °C in N<sub>2</sub> atmosphere. A total of 0.5 and/or 1.33 g of CS was dissolved in 200 mL of 2 wt% CH<sub>3</sub>COOH solution. An amount of 5 mL of Na<sub>2</sub>PdCl<sub>4</sub> solution (containing 0.09 mmol of Pd) was added dropwise into the

CS solution. A total of 2 g of the resultant TiO<sub>2</sub>-modified MMT was added into 200 mL of the above CS or CS-Pd<sup>2+</sup> complex solution, and continuously stirred at 60 °C (water-bath heating) for 10 h. The TiO<sub>2</sub>-MMT/CS or TiO<sub>2</sub>-MMT/CS@Pd<sup>2+</sup> products were separated from the suspension by centrifugation. After washing with deionized water to neutral and naturally drying, the TiO<sub>2</sub>-MMT/CS or TiO<sub>2</sub>-MMT/CS@Pd<sup>2+</sup> was carbonized into TiO<sub>2</sub>-MMT/PCN or TiO<sub>2</sub>-MMT/PCN@Pd<sup>2+</sup> at 800 °C for 4 h under N<sub>2</sub> atmosphere in the tubular muffle furnace. Before catalytic use, the resultant TiO<sub>2</sub>-MMT/PCN@Pd was further reduced with ethylene glycol at 80 °C for about 1 h to obtain TiO<sub>2</sub>-MMT/PCN@Pd<sup>0</sup>. The nanocomposites were labelled according to the mass ratio of the TiO<sub>2</sub>-MMT to CS (i.e., 80/20, and 60/40), such as TiO<sub>2</sub>-MMT<sub>80</sub>/PCN<sub>20</sub>, MMT<sub>60</sub>/PCN<sub>40</sub>, TiO<sub>2</sub>-MMT<sub>80</sub>/PCN<sub>20</sub>@Pd<sup>2+</sup>, TiO<sub>2</sub>-MMT<sub>80</sub>/PCN<sub>20</sub>@Pd<sup>0</sup>, TiO<sub>2</sub>-MMT<sub>60</sub>/PCN<sub>40</sub>@Pd<sup>2+</sup>, and TiO<sub>2</sub>-MMT<sub>60</sub>/PCN<sub>40</sub>@Pd<sup>0</sup>, respectively. For comparing the catalytic performances, Pd<sup>0</sup> immobilized on TiO<sub>2</sub>, PCN, TiO<sub>2</sub>/PCN, MMT/PCN, TiO<sub>2</sub>-MMT were also prepared, and the preparing process is shown in the supporting file.

**Characterizations:** X-ray diffraction (XRD) patterns of the samples with  $2\theta$  from 2–10° (small angle) and 10–60° (wide angle) were recorded using a Bruker D8 Advance (Bruker Corporation, USA) with a scanning rate of 1°/min, employing Cu K $\alpha$  radiation ( $\lambda = 0.154$  nm). N<sub>2</sub> adsorption–desorption isotherms of the samples were recorded using a Micromeritics TriStar II 3020 apparatus (Micromeritics Company, USA) at the liquid N<sub>2</sub> temperature of 77 K. Before the N<sub>2</sub> adsorption–desorption isotherms test, the samples were degassed at 200 °C for 6 h. The BET measurements were repeated 3 times. Morphology of the samples was observed using a JEM-2100 F high-resolution transmission electron microscope HRTEM (JEOL Ltd., Tokyo, Japan) equipped with an energy-dispersive X-ray-spectroscopy (Oxford EDX system). The HRTEM samples were firstly dispersed in ethanol in an ultrasonic bath for 5–10 min, and then deposited on a Cu grid and dried at room temperature. The samples were also observed with a scanning electron microscope SEM (JEM-6360, JEOL Ltd. Japan) equipped with an energy-dispersive X-ray spectroscopy (Oxford EDX system). Raman shifts of the samples were recorded using a DXR Raman Imaging Microscope (Thermo Scientific, USA) with excitation laser wavelength of 532 nm. Fourier transform infrared spectroscopy (FTIR) analysis of the samples was performed with a Thermo-Nicolet 470 FT-IR (USA) spectrometer (scans: 75 times/second; resolution: better than 0.09 cm<sup>-1</sup>) under the wave number ranging from 4000 to 400 cm<sup>-1</sup>, using KBr pressed-disk method. The mass ratio of the sample/KBr is about 1/100. Binding energies of the elements were determined using a Thermo Scientific ESCALAB 250Xi X-ray photoelectron spectrometer (USA). Pd content of the catalyst was determined with a Leemann ICP-AES Prodigy XP inductively coupled plasma-atomic emission spectrometer (USA). Samples for ICP-AES experiments were pre-treated with a mixed solution of concentrated HCl/fuming HNO<sub>3</sub> (3/1) and then diluted. Positron annihilation lifetime spectroscopy analysis of the samples was performed with an EG&G ORTEC fast–slow system (US). <sup>22</sup>Na (16  $\mu$ Ci) was used as positron source and the time resolution of the measurements was 190–220 ps. The total counts of lifetime spectrum of each sample were at least  $2 \times 10^6$ . Lifetime spectrum of each sample was resolved with the Lifetime 9.0 program.

**Catalysis applications:** The activity of the catalysts for the Sonogashira reactions was tested. A total of 1 mmol of aryl halide, 1.2 mmol of alkyne, TiO<sub>2</sub>-MMT/PCN@Pd<sup>0</sup> nanocomposites (containing about 2  $\mu$ mol of Pd<sup>0</sup>), 3 mmol of CH<sub>3</sub>COOK base, 0.2 mL of ethylene glycol, and 5 mL of dimethyl sulfoxide (DMSO) solvent was mixed in a 50 mL reaction tube with magnetic stirring for 3 h at 110 °C (oil-bath heating). The <sup>1</sup>H NMR spectra of each reaction product were determined with a Bruker 400-Hz NMR to verify the chemical structures, which were consistent with our previous studies [23,38,42]. Reaction yields of the reactions were based on the GC/MS measurements. The recyclability of the catalyst was evaluated with a model reaction of iodo benzene with phenyl acetylene. After each run, catalysts were separated and rinsed with ethanol. Afterwards, the recycled catalysts were reused in the next model reaction run.

**Adsorption tests:** Prior to the test, a calibration curve was obtained using the standard rhodamine B solution with known concentrations of 1, 2, 4, 6, 8, 10, 12, 14, 16 mg/L determined with a UV-vis spectrophotometer (UV-754, Shanghai) at an absorbance wavelength of 554 nm. At room temperature, 0.05 g TiO<sub>2</sub>-MMT<sub>80</sub>/PCN<sub>20</sub>@Pd<sup>0</sup> or TiO<sub>2</sub>-MMT<sub>60</sub>/PCN<sub>40</sub>@Pd<sup>0</sup> nanocomposite was added into the 100 mL of 50 mg/L rhodamine B solution under stirring. After specific time intervals of 10, 20, 30, 40, 50, 60 min, the sample solutions were filtered to determine the residual concentrations with UV-vis spectrophotometer using a calibration curve. The dye removal rate at time *t* (%) was calculated as  $(C_0 - C_t)/C_0 \times 100\%$ , where *C*<sub>0</sub> was the initial concentration of the dye solution, and *C*<sub>*t*</sub> was the concentration of the dye solution at time *t*.

#### 4. Conclusions

In summary, a combination of three catalyst supports of MMT clay, TiO<sub>2</sub>, and PCN into a hybrid system for stabilizing Pd species achieved a synergistic improvement of the comprehensive performance of the catalyst for Sonogashira reactions. The microstructure of the TiO<sub>2</sub>-MMT<sub>60</sub>/PCN<sub>40</sub>@Pd<sup>0</sup> nanocomposite was carefully characterized using XRD, N<sub>2</sub>-adsorption, and TEM, etc. The TiO<sub>2</sub>-pillaring modification can effectively improve the mesoporous structure of MMT. In situ PCN derived from CS was well engaged in the enlarged layer spaces of the MMT. The PALS analysis sensitively detected the development of sub-nano level microdefects during the preparation and recycling process of the catalytic nanocomposites. The successful incorporation of the TiO<sub>2</sub>, Pd, and PCN species within the interlayer nanospace of MMT was well reflected by the changes in the microdefects' information from the PALS analysis. In addition, after continuous long-term recovery, many newly developed large-sized microdefects were sensitively detected in the PALS analysis. Correspondingly, the four-lifetime fitting was more appropriate than the usual three-lifetime fitting for the analysis of the recovered catalysts. This study provided direct and instructive evidence for the decrease in the catalytic performance of recycled heterogeneous catalysts after long-term service from the aspect of sub-nano level microdefects.

**Supplementary Materials:** The following supporting information can be downloaded at: <https://www.mdpi.com/article/10.3390/molecules28052399/s1>, Figure S1: SEM-EDX scanning results of the TiO<sub>2</sub>-MMT<sub>60</sub>/PCN<sub>40</sub>@Pd<sup>0</sup> nanocomposites; Figure S2: N<sub>2</sub> adsorption–desorption isotherms of the heterogeneous catalysts; Figure S3: Performance of the heterogeneous catalysts applied in model Sonogashira reaction: A. Coupling yields vs time; B. Coupling yields vs recycling runs; Table S1: Structure parameter of heterogeneous catalysts extracted from the isotherms in Figure S2; Table S2: Model Sonogashira coupling reaction between iodo benzene and phenyl acetylene catalyzed using the heterogeneous catalysts; Table S3: A comparison of TiO<sub>2</sub>-MMT/PCN@Pd<sup>0</sup> catalyst with recently reported catalysts in Sonogashira reactions.

**Author Contributions:** Conceptualization, M.Z., B.W.; investigation, Y.C., K.S., T.Z., J.Z. and Y.L.; writing—original draft preparation, Y.C., Z.Y. and M.Z.; methodology, P.Z., X.R. and R.F.; writing—review and editing, M.Z.; visualization, Y.C.; supervision, Z.Y., X.C. and M.Z.; project administration, M.Z. All authors have read and agreed to the published version of the manuscript.

**Funding:** This research was funded by the National Natural Science Foundation of China (Grant No. 11875193, 12175149, 11475114); the Zhejiang Provincial Fundamental Public Welfare Research Project of China (Grant No. LGG18E030004); and the Shaoxing Key Science and Technology Innovation Team Project.

**Institutional Review Board Statement:** Not applicable.

**Informed Consent Statement:** Not applicable.

**Data Availability Statement:** Data are available from authors based on reasonable requirement from readers.

**Conflicts of Interest:** The authors declare no conflict of interest.

**Sample Availability:** Samples of the compounds are not available from the authors.

## References

1. Pagliaro, M.; Pandarus, V.; Ciriminna, B.R.F.; Cara, P.D. Heterogeneous versus homogeneous palladium catalysts for cross-coupling reactions. *ChemCatChem* **2012**, *4*, 432–445. [[CrossRef](#)]
2. Muimhneacháin, E.Ó.; McGlacken, G.P. Pd (0) nanoparticles (NPs) as catalysts in cross-coupling reactions and the homogeneous vs. heterogeneous debate. In *Organometallic Chemistry*; The Royal Society of Chemistry: London, UK, 2015; pp. 33–53.
3. Hussain, I.; Capricho, J.; Yawer, M.A. Synthesis of biaryls via ligand-free Suzuki-Miyaura cross-coupling reactions: A review of homogeneous and heterogeneous catalytic developments. *Adv. Syn. Catal.* **2016**, *358*, 3320–3349. [[CrossRef](#)]
4. Gärtner, D.; Sandl, S.; von Wangelin, A.J. Homogeneous vs. heterogeneous: Mechanistic insights into iron group metal-catalyzed reductions from poisoning experiments. *Catal. Sci. Technol.* **2020**, *10*, 3502–3514. [[CrossRef](#)]
5. Zhao, M.; Wu, Y.; Cao, J.-P. Carbon-based material-supported palladium nanocatalysts in coupling reactions: Discussion on their stability and heterogeneity. *Appl. Organomet. Chem.* **2020**, *34*, e5539. [[CrossRef](#)]
6. Bej, A.; Ghosh, K.; Sarkar, A.; Knight, D.W. Palladium nanoparticles in the catalysis of coupling reactions. *RSC Adv.* **2016**, *6*, 11446–11453. [[CrossRef](#)]
7. Liu, X.; Astruc, D. Development of the applications of palladium on charcoal in organic synthesis. *Adv. Synth. Catal.* **2018**, *360*, 3426–3459. [[CrossRef](#)]
8. Díaz-Sánchez, M.; Díaz-García, D.; Prashar, S.; Gómez-Ruiz, S. Palladium nanoparticles supported on silica, alumina or titania: Greener alternatives for Suzuki–Miyaura and other C–C coupling reactions. *Environ. Chem. Lett.* **2019**, *17*, 1585–1602. [[CrossRef](#)]
9. Cartagena, D.; Bachmann, S.; Püntener, K.; Scalone, M.; Newton, M.A.; Esteves, F.A.P.; Rohrbach, T.; Zimmermann, P.P.; van Bokhoven, J.A.; Ranocchiaro, M. Highly selective Suzuki reaction catalysed by a molecular Pd–P-MOF catalyst under mild conditions: Role of ligands and palladium speciation. *Catal. Sci. Technol.* **2022**, *12*, 954–961. [[CrossRef](#)]
10. Okumura, K.; Iiyoshi, H. Spontaneous formation and catalysis of highly dispersed Pd0 on\* BEA zeolite. *Microporous Mesoporous Mater.* **2021**, *325*, 111336. [[CrossRef](#)]
11. Gawande, M.B.; Branco, P.S.; Varma, R.S. Nano-magnetite (Fe<sub>3</sub>O<sub>4</sub>) as a support for recyclable catalysts in the development of sustainable methodologies. *Chem. Soc. Rev.* **2013**, *42*, 3371–3393. [[CrossRef](#)]
12. Sadjadi, S.; Heravi, M.M.; Kazemi, S.S. Ionic liquid decorated chitosan hybridized with clay: A novel support for immobilizing Pd nanoparticles. *Carbohydr. Polym.* **2018**, *200*, 183–190. [[CrossRef](#)]
13. Wang, K.; Cui, W.; Bian, Z.; Liu, Y.; Jiang, S.; Zhou, Y.; Wang, J. Size and stability modulation of Pd nanoparticles on porous hypercrosslinked ionic polymer for heterogeneous aerobic oxidative coupling of diaryl ether. *Appl. Catal. B Environ.* **2021**, *281*, 119425. [[CrossRef](#)]
14. Silva, T.L.; Ronix, A.; Pezoti, O.; Souza, L.S.; Leandro, P.K.; Bedin, K.C.; Beltrame, K.K.; Cazetta, A.L.; Almeida, V.C. Mesoporous activated carbon from industrial laundry sewage sludge: Adsorption studies of reactive dye Remazol Brilliant Blue R. *Chem. Eng. J.* **2016**, *303*, 467–476. [[CrossRef](#)]
15. Xu, J.; Liu, Y.; Tao, F.; Sun, Y. Kinetics and reaction pathway of Aroclor 1254 removal by novel bimetallic catalysts supported on activated carbon. *Sci. Total Environ.* **2019**, *651*, 749–755. [[CrossRef](#)]
16. Zeng, M.; Wang, Y.; Liu, Q.; Yuan, X.; Feng, R.; Yang, Z.; Qi, C. N-doped mesoporous carbons supported palladium catalysts prepared from chitosan/silica/palladium gel beads. *Int. J. Biol. Macromol.* **2016**, *89*, 449–455. [[CrossRef](#)]
17. Yang, S.; Chen, Y.; Huang, S.; Deng, L.; Wu, Y.; Zheng, X.; Omonov, S.; Zeng, M. Gelatin-pyrolyzed mesoporous N-doped carbon supported Pd as high-performance catalysts for aqueous Heck reactions. *Appl. Organomet. Chem.* **2021**, *35*, e6285. [[CrossRef](#)]
18. Xu, M.; Zhao, J.; Shu, G.; Zheng, X.; Liu, Q.; Wang, Y.; Zeng, M. One-pot carbonization of chitosan/P123/PdCl<sub>2</sub> blend hydrogel membranes to N-doped carbon supported Pd catalytic composites for Ullmann reactions. *Int. J. Biol. Macromol.* **2019**, *125*, 213–220. [[CrossRef](#)]
19. Chen, X.Y.; Chen, C.; Zhang, Z.J.; Xie, D.H. Gelatin-derived nitrogen-doped porous carbon via a dual-template carbonization method for high performance supercapacitors. *J. Mater. Chem. A* **2013**, *1*, 10903–10911. [[CrossRef](#)]
20. Zhao, X.; Tuo, B.; Long, S.; Song, X.; Wan, L.; Xiang, H. Study on adsorption of Cd<sup>2+</sup> by Ti-pillared montmorillonite-mixed activated carbon. *Micro Nano Lett.* **2021**, *16*, 304–312. [[CrossRef](#)]
21. Ikeue, K.; Mizukami, S.; Kuroda, A.; Hamada, S.; Hongo, A.; Masato, M. Noble-metal-containing nanoporous carbon synthesized within the interlayer space of montmorillonite and its catalytic property. *Appl. Catal. Gen.* **2008**, *351*, 68–74. [[CrossRef](#)]
22. Fan, X.; Yu, C.; Yang, J.; Ling, Z.; Hu, C.; Zhang, M.; Qiu, J. A layered-nanospace-confinement strategy for the synthesis of two-dimensional porous carbon nanosheets for high-rate performance supercapacitors. *Adv. Energy Mater.* **2015**, *5*, 1401761. [[CrossRef](#)]
23. Zeng, M.; Yang, S.; Chen, Y.; Xu, M.; Zhao, J.; Zhang, T.; Sun, K.; Yang, Z.; Zhang, P.; Cao, X.; et al. Porous chitosan-derived activated N-doped carbon-supported Pd nanoparticles encaged in Al, Fe pillared montmorillonite as novel heterogeneous catalysts. *Appl. Clay Sci.* **2022**, *224*, 106520. [[CrossRef](#)]
24. Slaný, M.; Jankovič, L.; Madejová, J. Structural characterization of organo-montmorillonites prepared from a series of primary alkylamines salts: Mid-IR and near-IR study. *Appl. Clay Sci.* **2019**, *176*, 11–20. [[CrossRef](#)]
25. Yin, J.; Pei, M.; He, Y.; Du, Y.; Guo, W.; Wang, L. Hydrothermal and activated synthesis of adsorbent montmorillonite supported porous carbon nanospheres for removal of methylene blue from waste water. *RSC Adv.* **2015**, *5*, 89839–89847. [[CrossRef](#)]
26. Tong, D.S.; Wu, C.W.; Adebajo, M.O.; Jin, G.C.; Yu, W.H.; Ji, S.F.; Zhou, C.H. Adsorption of methylene blue from aqueous solution onto porous cellulose-derived carbon/montmorillonite nanocomposites. *Appl. Clay Sci.* **2018**, *161*, 256–264. [[CrossRef](#)]

27. Ababneh, H.; Hameed, B. Chitosan-derived hydrothermally carbonized materials and its applications: A review of recent literature. *Int. J. Biol. Macromol.* **2021**, *186*, 314–327. [[CrossRef](#)]
28. Ahmed, M.; Hameed, B.; Hummadi, E. Review on recent progress in chitosan/chitin-carbonaceous material composites for the adsorption of water pollutants. *Carbohydr. Polym.* **2020**, *247*, 116690. [[CrossRef](#)]
29. Huang, S.; Yang, S.; Chen, Y.; Yang, Z.; Deng, L.; Wu, Y.; Zhang, T.; Feng, R.; Zeng, M. Porous carbon supported Pd catalysts derived from gelatin-based/chitosan or polyvinyl pyrrolidone/PdCl<sub>2</sub> blends. *J. Appl. Polym. Sci.* **2022**, *139*, 52163. [[CrossRef](#)]
30. Wang, Y.; Liu, Q.; Xu, M.; Shu, G.; Jiang, M.; Fei, G.; Zeng, M. Carbonization of chitosan in palladium-chitosan/montmorillonite composites to prepare novel heterogeneous catalysts for Heck reactions. *J. Macromol. Sci. Part B* **2017**, *56*, 670–681. [[CrossRef](#)]
31. Gil, A.; Korili, S.A.; Trujillano, R.; Vicente, M.A. A review on characterization of pillared clays by specific techniques. *Appl. Clay Sci.* **2011**, *53*, 97–105. [[CrossRef](#)]
32. Cardona, Y.; Vicente, M.A.; Korili, S.A.; Gil, A. Progress and perspectives for the use of pillared clays as adsorbents for organic compounds in aqueous solution. *Rev. Chem. Eng.* **2022**, *38*, 301–325. [[CrossRef](#)]
33. Cardona, Y.; Korili, S.A.; Gil, A. Understanding the formation of Al13 and Al30 polycations to the development of microporous materials based on Al13-and Al30-PILC montmorillonites: A review. *Appl. Clay Sci.* **2021**, *203*, 105996. [[CrossRef](#)]
34. Pandey, P.; Saini, V.K. Pillared interlayered clays: Sustainable materials for pollution abatement. *Environ. Chem. Lett.* **2019**, *17*, 721–727. [[CrossRef](#)]
35. Rezala, H.; Khalaf, H.; Valverde, J.L.; Romero, A.; Molinari, A.; Maldotti, A. Photocatalysis with Ti-pillared clays for the oxofunctionalization of alkyaromatics by O<sub>2</sub>. *Appl. Catal. Gen.* **2009**, *352*, 234–242. [[CrossRef](#)]
36. Kang, L.; Liu, H.; He, H.; Yang, C. Oxidative desulfurization of dibenzothiophene using molybdenum catalyst supported on Ti-pillared montmorillonite and separation of sulfones by filtration. *Fuel* **2018**, *234*, 1229–1237. [[CrossRef](#)]
37. Chen, K.; Li, J.; Li, J.; Zhang, Y.; Wang, W. Synthesis and characterization of TiO<sub>2</sub>-montmorillonites doped with vanadium and/or carbon and their application for the photodegradation of sulphorhodamine B under UV-vis irradiation. *Colloids Surf. Physicochem. Eng. Asp.* **2010**, *360*, 47–56. [[CrossRef](#)]
38. Chauhan, M.; Saini, V.K.; Suthar, S. Ti-pillared montmorillonite clay for adsorptive removal of amoxicillin, imipramine, diclofenac-sodium, and paracetamol from water. *J. Hazard. Mater.* **2020**, *399*, 122832. [[CrossRef](#)] [[PubMed](#)]
39. Zheng, X.; Zhao, J.; Liu, Q.; Xu, M.; Yang, S.; Zeng, M.; Qi, C.; Cao, X.; Wang, B. Chitosan modified Ti-PILC supported PdOx catalysts for coupling reactions of aryl halides with terminal alkynes. *Int. J. Biol. Macromol.* **2020**, *158*, 67–74. [[CrossRef](#)] [[PubMed](#)]
40. Hsing, J.; Kameshima, Y.; Nishimoto, S.; Miyake, M. Preparation of carbon-modified N-TiO<sub>2</sub>/montmorillonite composite with high photocatalytic activity under visible light radiation. *J. Ceram. Soc. Jpn.* **2018**, *126*, 230–235. [[CrossRef](#)]
41. Wang, L.; Zhang, B.; Meng, X.; Su, D.S.; Xiao, F.-S. Hydrogenation of Biofuels with Formic Acid over a Palladium-Based Ternary Catalyst with Two Types of Active Sites. *ChemSusChem* **2014**, *7*, 1537–1541. [[CrossRef](#)]
42. Chen, Y.; Yang, S.; Zhang, T.; Xu, M.; Zhao, J.; Zeng, M.; Sun, K.; Feng, R.; Yang, Z.; Zhang, P.; et al. Positron annihilation study of chitosan and its derived carbon/pillared montmorillonite clay stabilized Pd species nanocomposites. *Polym. Test.* **2022**, *114*, 107689. [[CrossRef](#)]
43. Zhao, J.; Zheng, X.; Liu, Q.; Xu, M.; Yang, S.; Zeng, M. Chitosan supported Pd<sup>0</sup> nanoparticles encaged in Al or Al-Fe pillared montmorillonite and their catalytic activities in Sonogashira coupling reactions. *Appl. Clay Sci.* **2020**, *195*, 105721. [[CrossRef](#)]
44. Alonso, D.A.; Baeza, A.; Chinchilla, R.; Gómez, C.; Guillena, G.; Pastor, I.M.; Ramón, D.J. Solid-Supported Palladium Catalysts in Sonogashira reactions: Recent developments. *Catalysts* **2018**, *8*, 202. [[CrossRef](#)]
45. Singha, S.; Sahoo, M.; Parida, K. Highly active Pd nanoparticles dispersed on amine functionalized layered double hydroxide for Suzuki coupling reaction. *Dalton Trans.* **2011**, *40*, 7130–7132. [[CrossRef](#)]
46. Darder, M.; Colilla, M.; Ruiz-Hitzky, E. Biopolymer-clay nanocomposites based on chitosan intercalated in montmorillonite. *Chem. Mater.* **2003**, *15*, 3774–3780. [[CrossRef](#)]
47. Schoonheydt, R.A.; Pinnavaia, T.; Lagaly, G.; Gangas, N. Pillared clays and pillared layered solids. *Pure Appl. Chem.* **1999**, *71*, 2367–2371. [[CrossRef](#)]
48. Lagaly, G. Characterization of clays by organic compounds. *Clay Miner.* **1981**, *16*, 1–21. [[CrossRef](#)]
49. Lagaly, G. Interaction of alkylamines with different types of layered compounds. *Solid State Ion.* **1986**, *22*, 43–51. [[CrossRef](#)]
50. Zha, C.; Wang, W.; Lu, Y.; Zhang, L. Constructing covalent interface in rubber/clay nanocomposite by combining structural modification and interlamellar silylation of montmorillonite. *ACS Appl. Mater. Interfaces* **2014**, *6*, 18769–18779. [[CrossRef](#)] [[PubMed](#)]
51. Liang, X.; Qi, F.; Liu, P.; Wei, G.; Su, X.; Ma, L.; He, H.; Lin, X.; Xi, Y.; Zhu, J.; et al. Performance of Ti-pillared montmorillonite supported Fe catalysts for toluene oxidation: The effect of Fe on catalytic activity. *Appl. Clay Sci.* **2016**, *132*, 96–104. [[CrossRef](#)]
52. Bakardjieva, S.; Šubrt, J.; Štengl, V.; Dianež, M.J.; Sayagues, M.J. Photoactivity of anatase-rutile TiO<sub>2</sub> nanocrystalline mixtures obtained by heat treatment of homogeneously precipitated anatase. *Appl. Catal. B Environ.* **2005**, *58*, 193–202. [[CrossRef](#)]
53. Hayati-Ashtiani, M. Use of FTIR spectroscopy in the characterization of natural and treated nanostructured bentonites (montmorillonites). *Part. Sci. Technol.* **2012**, *30*, 553–564. [[CrossRef](#)]
54. Zhang, Y.; Song, S.; Zhang, M.; Tuo, B. Preparation and characterization of titania-pillared montmorillonite. *Surf. Rev. Lett.* **2008**, *15*, 329–336. [[CrossRef](#)]
55. Chen, D.; Zhu, Q.; Zhou, F.; Deng, X.; Li, F. Synthesis and photocatalytic performances of the TiO<sub>2</sub> pillared montmorillonite. *J. Hazard. Mater.* **2012**, *235*, 186–193. [[CrossRef](#)]

56. Khan, A.; Nurnabi, M.; Bala, P. Studies on thermal transformation of Na-montmorillonite-glycine intercalation compounds. *J. Therm. Anal. Calorim.* **2009**, *96*, 929–935. [[CrossRef](#)]
57. Wagner, C.; Riggs, W.; Davis, L.; Moulder, J.; Muilenberg, G. *Handbook of X-ray Photoelectron Spectroscopy*; Perkin-Elmer Corp.: Eden Prairie, MN, USA, 1979; Volume 38.
58. Ding, M.; Zuo, S.; Qi, C. Preparation and characterization of novel composite AlCr-pillared clays and preliminary investigation for benzene adsorption. *Appl. Clay Sci.* **2015**, *115*, 9–16. [[CrossRef](#)]
59. Shufeng, Z.; Renxian, Z.; Chenze, Q. Synthesis and characterization of aluminum and Al/REE pillared clays and supported palladium catalysts for benzene oxidation. *J. Rare Earths* **2011**, *29*, 52–57.
60. Shen, B.; Chen, J.; Yue, S. Removal of elemental mercury by titanium pillared clay impregnated with potassium iodine. *Microporous Mesoporous Mater.* **2015**, *203*, 216–223. [[CrossRef](#)]
61. Zeng, M.; Zheng, X.; Wang, Y.; Shu, G.; Zhao, J.; Xu, M.; Qi, C.; Cao, X.; Wang, B. Investigation of organophilic montmorillonites supported palladium catalytic composites by combined positron annihilation lifetime spectroscopy and X-ray diffraction. *Radiat. Phys. Chem.* **2019**, *165*, 108343. [[CrossRef](#)]
62. Zhao, J.; Xu, M.; Shu, G.; Yang, Z.; Liu, Q.; Zeng, M.; Qi, C.; Cao, X.; Wang, B. Positron annihilation characteristics and catalytic performances of poly (vinyl alcohol) intercalated montmorillonite supported Pd0 nanoparticles composites. *Radiat. Phys. Chem.* **2018**, *153*, 164–172. [[CrossRef](#)]
63. Zheng, X.; Xu, M.; Yang, S.; Omonov, S.; Huang, S.; Zhao, J.; Ruan, H.; Zeng, M. Novel bio-inspired three-dimensional nanocomposites based on montmorillonite and chitosan. *Int. J. Biol. Macromol.* **2020**, *165*, 2702–2710. [[CrossRef](#)] [[PubMed](#)]
64. Joshi, J.; Sodaye, H.; Pujari, P.; Srisaila, S.; Bajpai, M. Positron annihilation spectroscopic investigation of Al-pillared montmorillonites. *Catal. Lett.* **1998**, *51*, 109–112. [[CrossRef](#)]
65. Sano, M.; Murakami, H.; Ichimura, K. Positronium in a layered-structure material: Montmorillonite. *J. Radioanal. Nucl. Chem.* **1999**, *239*, 325–328. [[CrossRef](#)]
66. Tao, S. Positronium annihilation in molecular substances. *J. Chem. Phys.* **1972**, *56*, 5499–5510. [[CrossRef](#)]
67. Eldrup, M.; Lightbody, D.; Sherwood, J.N. The temperature dependence of positron lifetimes in solid pivalic acid. *Chem. Phys.* **1981**, *63*, 51–58. [[CrossRef](#)]
68. Consolati, G.; Natali-Sora, I.; Pelosato, R.; Quasso, F. Investigation of cation-exchanged montmorillonites by combined X-ray diffraction and positron annihilation lifetime spectroscopy. *J. Appl. Phys.* **2002**, *91*, 1928–1932. [[CrossRef](#)]
69. Jasińska, B.; Koziol, A.; Goworek, T. Void shapes and o-Ps lifetime in molecular crystals. *Acta Phys. Pol. A* **1999**, *95*, 557–561. [[CrossRef](#)]
70. Tabassum, S.; Zahoor, A.F.; Ahmad, S.; Noreen, R.; Khan, S.G.; Ahmad, H. Cross-coupling reactions towards the synthesis of natural products. *Mol. Divers.* **2022**, *26*, 647–689. [[CrossRef](#)]
71. Rayadurgam, J.; Sana, S.; Sasikumar, M.; Gu, Q. Palladium catalyzed C–C and C–N bond forming reactions: An update on the synthesis of pharmaceuticals from 2015–2020. *Org. Chem. Front.* **2021**, *8*, 384–414. [[CrossRef](#)]
72. Hong, K.; Sajjadi, M.; Suh, J.M.; Zhang, K.; Nasrollahzadeh, M.; Jang, H.W.; Varma, R.S.; Shokouhimehr, M. Palladium nanoparticles on assorted nanostructured supports: Applications for Suzuki, Heck, and Sonogashira cross-coupling reactions. *ACS Appl. Nano Mater.* **2020**, *3*, 2070–2103. [[CrossRef](#)]
73. Sun, S.; Li, H.; Xu, Z.J. Impact of surface area in evaluation of catalyst activity. *Joule* **2018**, *2*, 1024–1027. [[CrossRef](#)]
74. Puskás, R.; Varga, T.; Grósz, A.; Sági, A.; Oszkó, A.; Kukovecz, Á.; Kónya, Z. Mesoporous carbon-supported Pd nanoparticles with high specific surface area for cyclohexene hydrogenation: Outstanding catalytic activity of NaOH-treated catalysts. *Surf. Sci.* **2016**, *648*, 114–119. [[CrossRef](#)]
75. Elhampour, A.; Nemati, F. Palladium nanoparticles supported on modified hollow-Fe<sub>3</sub>O<sub>4</sub>@TiO<sub>2</sub>: Catalytic activity in Heck and Sonogashira cross coupling reactions. *Org. Prep. Proced. Int.* **2017**, *49*, 443–458. [[CrossRef](#)]
76. Eskandari, A.; Jafarpour, M.; Rezaeifard, A.; Salimi, M. Supramolecular photocatalyst of Palladium (II) Encapsulated within Dendrimer on TiO<sub>2</sub> nanoparticles for Photo-induced Suzuki-Miyaura and Sonogashira Cross-Coupling reactions. *Appl. Organomet. Chem.* **2019**, *33*, e5093. [[CrossRef](#)]
77. Chavan, S.P.; Varadwaj, G.B.B.; Parida, K.; Bhanage, B.M. Palladium anchored on amine-functionalized K10 as an efficient, heterogeneous and reusable catalyst for carbonylative Sonogashira reaction. *Appl. Catal. Gen.* **2015**, *506*, 237–245. [[CrossRef](#)]
78. Liu, Q.; Xu, M.; Zhao, J.; Yang, Z.; Qi, C.; Zeng, M.; Xia, R.; Cao, X.; Wang, B. Microstructure and catalytic performances of chitosan intercalated montmorillonite supported palladium (0) and copper (II) catalysts for Sonogashira reactions. *Int. J. Biol. Macromol.* **2018**, *113*, 1308–1315. [[CrossRef](#)] [[PubMed](#)]
79. Modak, A.; Bhaumik, A. Surface-exposed Pd nanoparticles supported over nanoporous carbon hollow tubes as an efficient heterogeneous catalyst for the CC bond formation and hydrogenation reactions. *J. Mol. Catal. Chem.* **2016**, *425*, 147–156. [[CrossRef](#)]
80. Sadjadi, S.; Lazzara, G.; Malmir, M.; Heravi, M.M. Pd nanoparticles immobilized on the poly-dopamine decorated halloysite nanotubes hybridized with N-doped porous carbon monolayer: A versatile catalyst for promoting Pd catalyzed reactions. *J. Catal.* **2018**, *366*, 245–257. [[CrossRef](#)]

**Disclaimer/Publisher's Note:** The statements, opinions and data contained in all publications are solely those of the individual author(s) and contributor(s) and not of MDPI and/or the editor(s). MDPI and/or the editor(s) disclaim responsibility for any injury to people or property resulting from any ideas, methods, instructions or products referred to in the content.